

NANOFLUIDIC SINGLE MOLECULE DETECTION (SMD) FOR PROTEIN
DETECTION AND INTERACTION DYNAMICS STUDY

A Dissertation

by

NAN JING

Submitted to the Office of Graduate Studies of
Texas A&M University
in partial fulfillment of the requirements for the degree of
DOCTOR OF PHILOSOPHY

May 2009

Major Subject: Electrical Engineering

NANOFLUIDIC SINGLE MOLECULE DETECTION (SMD) FOR PROTEIN
DETECTION AND INTERACTION DYNAMICS STUDY

A Dissertation

by

NAN JING

Submitted to the Office of Graduate Studies of
Texas A&M University
in partial fulfillment of the requirements for the degree of

DOCTOR OF PHILOSOPHY

Approved by:

Chair of Committee,	Jun Kameoka
Committee Members,	Chin B. Su
	Steven Wright
	Kuang-An Chang
Head of Department,	Costas N. Georghiadis

May 2009

Major Subject: Electrical Engineering

ABSTRACT

Nanofluidic Single Molecule Detection (SMD) for Protein Detection and Interaction
Dynamics Study. (May 2009)

Nan Jing, B.S., Southeast University, Nanjing, China; M.S., Case Western Reserve
University

Chair of Advisory Committee: Dr. Jun Kameoka

The objective of this work is to develop a micro/nanofluidic-based single molecule detection (SMD) scheme, which would allow us to inspect individual protein or protein complex study protein-protein interactions and their dynamics. This is a collaboration work with MD Anderson Cancer Center and we applied this scheme to study functions of various proteins related to cancer progression in hope to shed new light on cancer research.

State-of-the-art micro/nano-fabrication technology is used to provide fused silica micro/nano-fluidic channel devices as our detection platform. Standard contact photolithography, projection photolithography and advanced electron-beam lithography are used to fabricate micro/nano-fluidic channel with width ranging from 100nm to 2 μ m. The dimensions of these miniaturized biochips are designed to ensure single molecule resolution during detection and shrinking the detection volume leads to increase in signal-to-noise ratio, which is very critical for SMD. To minimize surface adsorption of

protein, a fused silica channel surface coating procedure is also developed and significantly improved the detection efficiency.

A fluorescent-labeled protein sample solution is filled in the fluidic channel by capillary force, and proteins are electro-kinetically driven through the fluidic channel with external voltage source. Commercial functionalized Quantum Dots (Qdots) are used as fluorescent labels due to its various advantages over conventional organic dyes for single molecule multi-color detection application. A fluorescence correlation spectrometer system, equipped with a 375nm diode laser, 60x water immersion objective with N.A. of 1.2 and two avalanche photodiodes (APD) is implemented to excite single molecules as well as collect emitted fluorescence signals.

A two-dimensional photon burst analysis technique (photon counts vs. burst width) is developed to analyze individual single molecule events. We are able to identify target protein or protein complex directly from cell lysate based on fluorescence photon counts, as well as study the dynamics of protein-protein interactions. More importantly, with this technique we are also able to assess interactions between three proteins, which cannot be done with current ensemble measurement techniques.

In summary, the technique described in this work has the advantages of high sensitivity, short processing time (2-3 minutes), very small sample consumption and high resolution quantitative analysis. It could potentially revolutionize the area of protein interaction research and provides us with more clues for the future of cancer diagnostics and treatments.

DEDICATION

To my parents and family

ACKNOWLEDGEMENTS

I would like to thank my advisor, Dr. Jun Kameoka, for his unrelenting guidance and support throughout the course of my research. I would also like to thank my committee members, Dr. Su, Dr. Wright and Dr. Chang, for their valuable insights and suggestions on my research.

This work is in collaboration with Mr. Chao-Kai Chou and Dr. Hung at the Department of Molecular and Cellular Oncology, MD Anderson Cancer Center. I'm very grateful for their help and support as well.

Thanks also go to my friends and colleagues and the department staff for making my time at Texas A&M University a great experience. I also want to extend my gratitude to the staff at Cornell Nanoscale Facility for their help on device fabrication, and to the staff at Microscopy Imaging Center and Materials Characterization Facility at Texas A&M University.

Last but not least, I want to thank my parents and brother for their love and encouragement. Without you, this could not be possible.

NOMENCLATURE

APD	Avalanche Photodiode
ASCII	American Standard Code for Information Interchange
CE	Capillary Electrophoresis
CNF	Cornell Nanoscale Facility
Co-IP	Co-Immunoprecipitation
CPS	Counts per Second
DI	De-Ionized
EBL	Electron Beam Lithography
EGFR	Epidermal Growth Factor Receptor
EOF	Electro-Osmotic Flow
FCS	Fluorescence Correlation Spectrometer
FLMAD	Flag (FL) Epitope Tagged MAD
HAMAX	Hemagglutinin (HA) Epitope Tagged MAX
IP	Immunoprecipitation
LIF	Laser Induce Fluorescence
MAD	MAX Dimerizer
MAX	MYC Associated Factor X
N. A.	Numerical Aperture
PDMS	Poly (dimethylsiloxane)
PEI	Polyethyleneimine

PMMA	Poly (methyl methacrylate)
RIE	Reactive Ion Etching
RPM	Revolutions per Minute
SCCM	Standard Cubic Centimeters per Minute
SEM	Scanning Electron Microscope
SMD	Single Molecule Detection
STAT3	Signal Transducer and Activator of Transcription 3

TABLE OF CONTENTS

	Page
ABSTRACT	iii
DEDICATION	v
ACKNOWLEDGEMENTS	vi
NOMENCLATURE.....	vii
TABLE OF CONTENTS	ix
LIST OF FIGURES.....	xii
LIST OF TABLES	xvii
1. INTRODUCTION.....	1
2. BACKGROUND.....	3
2.1 Fluorescence single molecule detection.....	3
2.2 Micro/nano-fluidic technology.....	5
2.2.1 Technology overview.....	5
2.2.2 Fabrication techniques.....	7
2.3 Micro/nano-fluidic single molecule detection.....	11
2.3.1 Technology overview.....	11
2.3.2 Molecule interaction study by micro/nano-fluidic SMD	12
2.4 Conventional protein detection and interaction study in cancer cell.....	13
2.4.1 Importance of protein interaction study in cancer research ...	13
2.4.2 Conventional protein detection and interaction assays	16
3. MICRO/NANO-FLUIDIC CHANNEL FABRICATION	19
3.1 Bulk fabrication of fused silica micro/nano-fluidic channel.....	19
3.1.1 Contact lithography for 2 μ m-wide microchannel	19
3.1.2 Projection lithography for 500nm-wide nanochannel	23
3.2 Surface modification of fused silica channel	25

	Page
4. MATERIALS	29
4.1 Quantum dots	29
4.2 Sample preparation.....	31
5. FLUORESCENCE SMD IN FLUIDIC CHANNEL	33
5.1 Experiment setup.....	33
5.2 Experiment procedure	36
5.3 Data analysis	39
5.3.1 Fluorescence correlation spectroscopy (FCS).....	39
5.3.2 Two-dimensional (2D) photon burst analysis	41
5.3.3 Dual-color photon burst coincidence analysis	44
6. MICROFLUIDIC TARGET PROTEIN DETECTION.....	47
6.1 Principle of detection	47
6.2 Qdots in microfluidic channel	49
6.3 Detection of HAMAX and its concentration analysis.....	52
7. NANOFLUIDIC PROTEIN INTERACTION STUDY	61
7.1 Principle of detection	61
7.1.1 One color scheme	61
7.1.2 Dual color scheme	62
7.2 Model protein	64
7.2.1 MAX-MAD interaction study by one color scheme	68
7.2.2 MYC-MAX interaction study by one color and dual color schemes	63
7.3 Cancer related protein	72
7.3.1 Detection of EGFR protein and concentration analysis	73
7.3.2 Dual-color detection of SRC-EGFR-STAT3 three-protein interaction --- a preliminary study	75
8. CONCLUSIONS AND FUTURE WORKS	84
8.1 Conclusions	84
8.2 Future works.....	87
REFERENCES	89
APPENDIX A	96

	Page
APPENDIX B	99
APPENDIX C	102
VITA	103

LIST OF FIGURES

	Page
Figure 1 Simplified three-state Jablonski diagram of a molecule's energetic states that are involved in its photophysics	5
Figure 2 Microfluidic bioreactor to monitor the populations of bacteria	7
Figure 3 Concept of photolithography.....	8
Figure 4 A typical lithography process to fabricate micro/nano-fluidic channel	9
Figure 5 Scanning electron microscope (SEM) images of nanofluidic channel device	11
Figure 6 Protein interaction study along one of the tumor signal pathways in breast cancer cell	15
Figure 7 Illustration of a typical immunoprecipitation (IP) process.....	17
Figure 8 Optical image of microfluidic channel with width of 2 μ m.....	22
Figure 9 Photo of a microchannel device after bonding.....	23
Figure 10 SEM image of microfluidic channel with width of 500nm.....	24
Figure 11 Fluorescence image of bare fused silica microchannel filled with QD525	26
Figure 12 Autocorrelation of QD525 in microchannel under 100V.....	27
Figure 13 Electro-kinetic bulk flow inside fused silica channel (PH~7).....	28
Figure 14 Structure of functionalized Qdot.....	29
Figure 15 Size dependable emission spectrum of Qdot.....	30

	Page
Figure 16 Photo of fluorescence correlation spectrometer system	33
Figure 17 Optical path of fluorescence correlation spectrometer system and detailed configuration parameters	34
Figure 18 Transmission spectrums of dichroic mirror and filter set implemented in dual channel system	35
Figure 19 Photo of microchannel device on microscope stage during detection	36
Figure 20 Development of an autocorrelation curve	40
Figure 21 Procedure of plotting 2D photon burst diagram	42
Figure 22 Effect of moving average method on photon burst signal	44
Figure 23 Principle of dual-color photon burst coincidence analysis to characterize the dynamics of protein-protein interaction	46
Figure 24 One-color single molecule flow proteometry	47
Figure 25 Target protein detection based on photon counts by using primary antibody of polyclonal nature	48
Figure 26 Autocorrelation of 1nM QD525 in microfluidic channel under external field ranging from 50V to 500V	50
Figure 27 Linear fit of QD525 flow velocity as a function of voltages at 50V, 100V, 200V, 300V and 500V	51
Figure 28 Linear fit of number of QD525 events identified (moving averaged) as a function of QD525 concentration	52

Figure 29	Linear fit of QD525-HAMAX flow velocity as a function of voltages at 50V, 100V, 200V, 300V and 500V	53
Figure 30	HAMAX photon burst as a function of time at 200V (A) and 500V (B), magnified peaks at 200V(C) and 500V (D)	54
Figure 31	Detection of HAMAX target protein	55
Figure 32	Photon burst peaks of pure QD525, vector and HAMAX sample at 200V with an integration time of 1 millisecond.....	56
Figure 33	Determination of photon burst and burst width of QD525 boundary at 200V	57
Figure 34	2D photon burst plots of HAMAX events from cell lysate of 1 μ g (A), 5 μ g (B) and 10 μ g (C) transfection DNA	58
Figure 35	HAMAX concentration analysis and normalized average number of HAMAX events as a function of transfection DNA amount	59
Figure 36	One-color protein interaction detection based on photon counts by using primary antibody of polyclonal nature	61
Figure 37	A dual-color fluorescence single molecule detection system for multiple protein interaction study and its coincidence analysis	63
Figure 38	QD525 and QD605 photon burst coincidence	65
Figure 39	2D photon burst diagram of QD525 (A) and HAMAX (B) at 200V	66
Figure 40	2D photon burst diagram of HAMAX-FLMAD and one-color detection of MAX-MAD interaction.....	67

	Page
Figure 41 2D photon burst diagram of HAMAX-MYC and one-color detection of MAX-MYC interaction	68
Figure 42 Detection principle of two-protein interaction (MYC-MAX) with dual-color photon burst coincidence analysis	69
Figure 43 Dual-color photon burst coincidence plot of vector cell lysate sample containing only QD525 and QD605	70
Figure 44 Dual-color photon burst coincidence plots of MYC (A) and HAMAX (B) samples.....	71
Figure 45 Dual-color photon burst coincidence analysis of MYC-MAX sample.....	72
Figure 46 Detection of target EGRF protein in different cells	73
Figure 47 EGFR concentration analysis	74
Figure 48 Detection principle of three-protein interaction (SRC-EGFR-STAT3) with dual-color photon burst coincidence analysis	76
Figure 49 2D photon burst analysis of STAT3 (B) and SRC (A) proteins and dual-color photon burst coincidence analysis of STAT3 (C) and SRC (D).....	80
Figure 50 Dual-color photon burst coincidence analysis of SRC/EGFR/STAT3 three-protein interaction	81

	Page
Figure 51 Interaction dynamics between SRC, EGFR and STAT3 proteins in HeLa tumor cell.....	82
Figure 52 2D photon burst diagrams of HAMAX sample with different lysate concentrations	99
Figure 53 Number of HAMAX events as a function of HAMAX lysate concentration.....	101

LIST OF TABLES

	Page
Table 1 SMD methods at room-temperature with potential use in biomolecular applications	4
Table 2 Comparison of Co-IP/western blot and micro/nano-fluidic SMD techniques for protein interaction study	18
Table 3 Typical microfabrication process flow of microfluidic device used in this study	20

1. INTRODUCTION

Breast cancer is the most common type of cancer among woman in this country. Despite advances in imaging and treatments, more than 40,000 women die because of breast cancer each year. In fact, the National Cancer Institute estimated that 13.4 percent of woman born today would be diagnosed with breast cancer at some time in their lives [1]. Cancer progression is caused by the deregulations of signal pathways and the signal transduction is carried out through physical interactions between various proteins. Prof. Hung's group at MD Anderson Cancer Center had put tremendous effort into dissecting the dynamic of signal transduction in breast cancer cell [2-5]. Various tumor-related proteins along the signal pathways were extensively studied. However, many details still remain obscure due to limitations of current techniques [6-8].

Most of the current molecule interaction assays are based on ensemble measurements. SMD, on the other hand, interrogates individual molecule with extremely high sensitivity and reveals valuable information, which could be masked by averaging in experiments performed on ensembles of molecules. However, to implement single molecule detection is not trivial as it needs a small detection volume, low analyte concentration, improved signal-to-noise ratio and extremely sensitive detector to achieve single molecule resolution.

This dissertation follows the style of *Lab on a Chip*.

In recent years, the rapid development of microfluidic technology provides SMD with a new platform, which offers considerable advantages over conventional bulk solution scheme.

The general techniques for protein interactions detection include immunoprecipitation, immuno-fluorescence staining, and fluorescence resonant energy transfer, etc. These assays usually require long processing time, large sample consumption and have inherent detection limitations. For example, current assays are usually used to detect interaction between two molecules. For a three-molecule interaction study, the “double” immuno-precipitation assay needs to be performed. However, this assay is a complicate and time-consuming procedure that accompany with detection limitations, let alone to demonstrate the population of different complexes. Furthermore, target molecule detection still relies on X-ray film exposure or eye-direct observation that may limit the sensitivity and accuracy of detection.

The nanofluidic single molecule detection technique described in this work is designed and developed to overcome these aforementioned limitations and provide rapid, accurate and sensitive protein complex interaction detection.

2. BACKGROUND

2.1 Fluorescence single molecule detection

Most conventional bio-analytical techniques utilize ensemble measurements and only yield information on the average for the entire population in a certain time frame. However we seldom deal with homogeneous samples, therefore, any fluctuation, reaction intermediate states and time trajectories of observables for a subpopulation within a heterogeneous system will be masked with ensemble measurements [9]. In other words, SMD techniques are able to provide us with invaluable information of molecular dynamics in many aspects that otherwise be hidden and sometimes impossible to obtain with conventional techniques [10]. For the work described here, we hope to use SMD techniques to collect information of individual molecules and at the same time, quantify different molecules of interest in a heterogeneous sample solution.

The first, indirect detection of a single molecule in solution was performed by Rotman in 1961 when detecting multiply reaction products of a single enzymatic molecule [11, 12]. Over the years, various SMD techniques have been developed and a summary of current optical SMD methods for biomolecule detection is presented in Table 1 [13]. Other non-optical based SMD techniques, including electron microscopy, scanning probe microscopy, mass spectroscopy, etc., have the disadvantages, such as lack-of-specificity, destructive, invasive detection for biomolecules, difficult to probe molecule in its native environment and complicated instrumentation compared to optical techniques [13]. Among optical SMD techniques, laser induced fluorescence (LIF) is

one of the most commonly used techniques for various reasons. The exquisite sensitivity and selectivity of emission spectroscopy is ideally suited to non-invasively probing the small volume and low analyte concentration with high throughput [14]. Furthermore, many conventional bio-analytical methods are fluorescent-based techniques and this technology, including fluorescent chemistry, labeling techniques, etc., had been established for quite some time and is readily available. In addition, the recent developments of laser technologies have expanded the low cost excitation sources that span the visible and infrared regions of the electromagnetic spectrum [14].

Table 1. SMD methods at room-temperature with potential use in biomolecular applications [13].

in fluids	laser induce fluorescence	fluid flow
		micro-capillary electrophoresis
		fluorescence correlation spectroscopy
		levitated micro-droplets
	laser induced Raman scattering	single molecules adsorbed on colloidal metal particles in solution
on surfaces	far-field methods	confocal microscopy
		wide-field fluorescence microscopy with low noise CCD cameras
	near-field methods	near-field scanning microscopy

The basic photophysics of LIF can be described by the Jablonski diagram as depicted in Figure 1. The nonexcited molecule resides in its electronic ground state S_0 . From there it can be excited by single- or multi-photon absorption into its first excited electronic state S_1 , from where it can either (1) return to its ground state S_0 , via emission of a fluorescence photon or by a non-radiative transition induced by the interaction with

the surrounding medium, (2) switch into a triplet state (T_1) via intersystem crossing, or (3) be irreversibly destroyed by a photochemical reaction (photobleaching) [12].

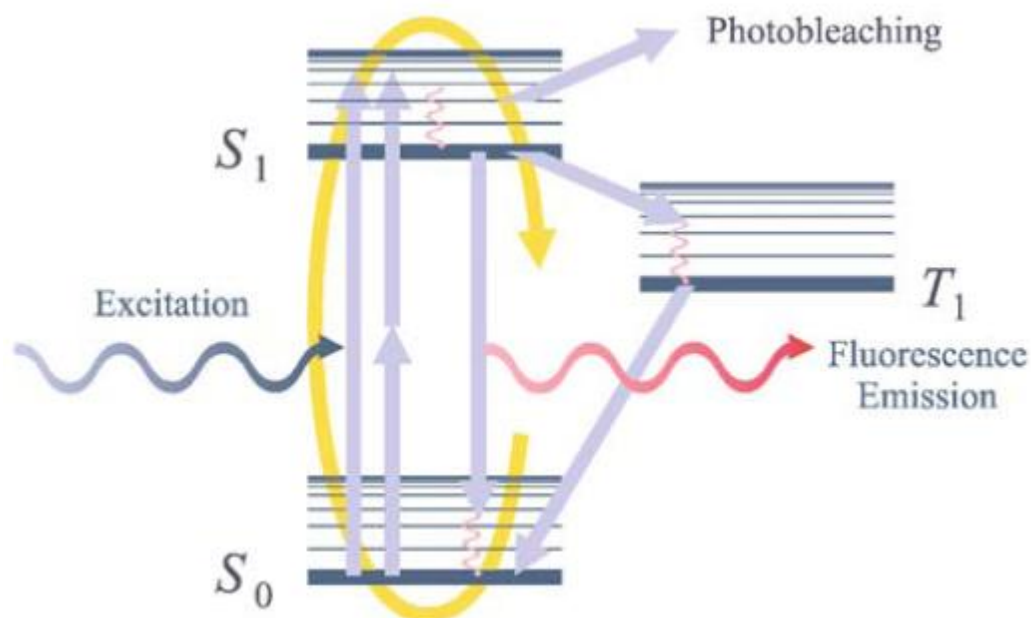


Figure 1 Simplified three-state Jablonski diagram of a molecule's energetic states that are involved in its photophysics [12].

2.2 Micro/nano-fluidic technology

2.2.1 Technology overview

The first successful detection of single molecule in solution was accomplished in a channel flowing environment [15]. With the rapid development of micro/nano-fluidic technology in the last two decades, more and more researchers are combining SMD with microfluidic technology to develop new applications or improve current methods in various bioscience and bio-analytical fields. In this section, a brief background of

micro/nano-fluidic technology is presented. Advantages and applications of micro/nanofluidic SMD will be discussed in detail in the next section.

Micro/nanofluidic is the science and technology of systems that process or manipulate small (10^{-9} to 10^{-18} liters) amounts of fluids, using channels with dimensions of tens to hundreds of micrometers or even nanometers range [16]. One of the first applications of microfluidic technology is on-chip capillary electrophoresis (CE) [17] in 1992 and compared to conventional CE, it offers advantages, such as very small samples and reagents consumption, separations and detections with high resolution and sensitivity, low-cost and short times for analysis [16]. This technology has received enormous recent attention because of (1) the rapid development of microfabrication technology, which allows fabrication of integrated flow systems with length scales on the order of tens to hundreds of microns down to nanometer range (2) rapid developments in biology and biotechnology for which manipulations on the cellular or even molecular length scale and the ability to detect small quantities and manipulate very small volumes offer advantages (3) the quest for cheap portable devices able to perform simple analytical tasks, and (4) the potential use of microfluidic systems to perform fundamental studies of physical, chemical, and biological processes [18]. An example of large scale integrated microfluidic device is showed in figure 2. It's a microfluidic bioreactor used to long-term culture and monitor extremely small populations of bacteria with single-cell resolution [19]. Although this technology is still at its early stage of development, it had already found applications in many areas, such as molecular biology (enzymatic analysis, DNA analysis and proteomics), examination

and manipulation of single cell for cell biology study, high-throughput drug screening, chemical synthesis, clinical pathology/diagnostics and bio-defense, just to name a few. For details on current microfluidic technology, applications and physics, there are a number of excellent reviews available in the literature [16, 18, 20-25].

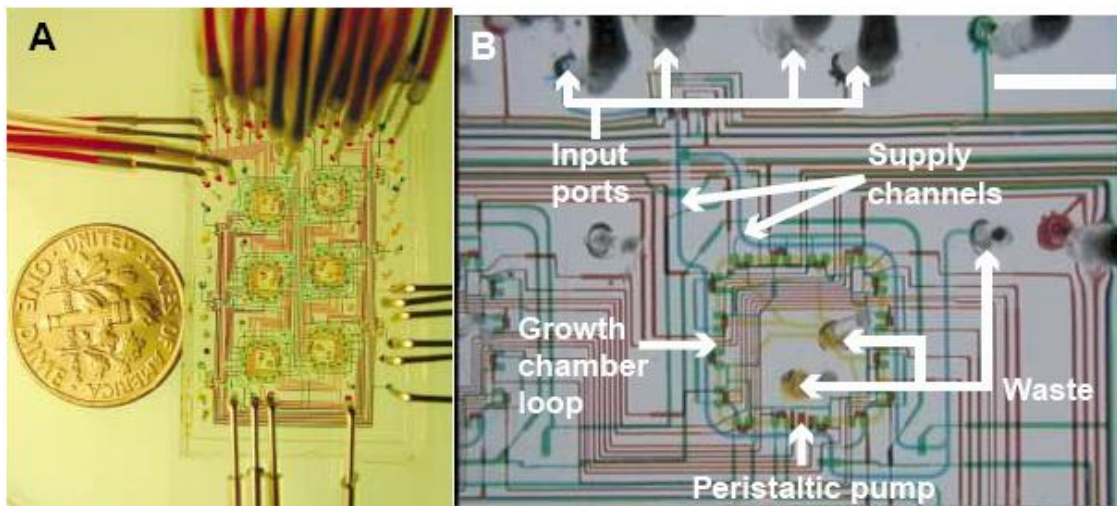


Figure 2 Microfluidic bioreactor to monitor the populations of bacteria. A) Photo of a real device. B) Each reactor consists of a growth chamber, which is a fluidic loop 10mm high, 14mm wide, and 11.5mm in circumference, with an integrated peristaltic pump and a series of micromechanical valves to add medium, remove waste, and recover cells.

Dye solutions were introduced into the channel for a better visualization [19].

2.2.2 Fabrication techniques

Microfabrication techniques and traditional silicon processing techniques are essential to the development of micro/nano-fluidic technology. Many integrated microfluidic systems contain functional elements including valves, pumps, actuators, switches, sensors, dispensers, mixers, filters, separators, heaters, etc. [18]. Fabrication and integration of these parts on micro- or even nano- scale are not trivial tasks and more

often than not, sophisticated microfabrication techniques are needed. In this section, a brief overview of micro/nanofluidic device fabrication techniques is presented. Basically, all the fabrication methods can be categorized into two groups and described as: *Top-down* and *Bottom-up*. In short, bottom-up approach is to have molecular components arrange themselves into more complex structures while top-down approach is to use larger and externally-controlled components to direct their assembly.

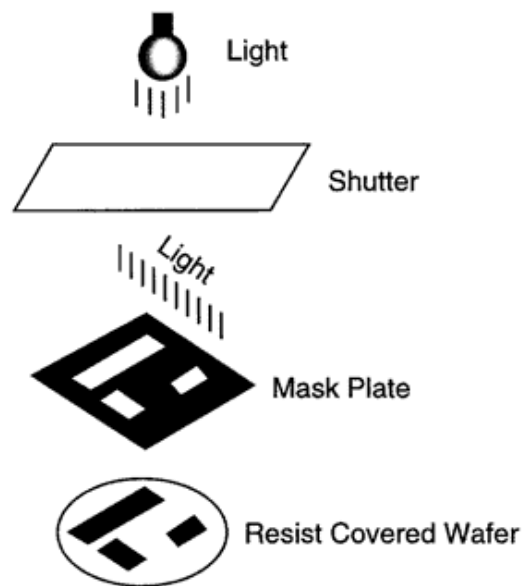


Figure 3 Concept of photolithography [26].

More often than not, top-down is being referred as lithography techniques and currently, it is considered as the most common and prevalent approach to fabricate micro/nano-fluidic devices. It relies heavily on silicon processing techniques developed for microelectronics and integrated circuit industry. The basic concept of photolithography is illustrated in figure 3. Firstly, substrate is coated with a thin film of

light-sensitive materials called photoresist. Then, a mask plate with transparent and opaque areas is brought close. Depending on the property of photoresist, designed features can be either transparent or opaque on the mask plate. The next step is to carefully align the mask plate with the substrate and expose the photoresist-coated substrate to an external light source with the mask plate in between. Upon light exposure, photoresist underneath the transparent part of the mask undergoes chemical reaction with the incoming light. Finally, exposed photoresist can either be removed from or remain on the substrate using special chemicals and the design features are thus being transferred onto the substrate.

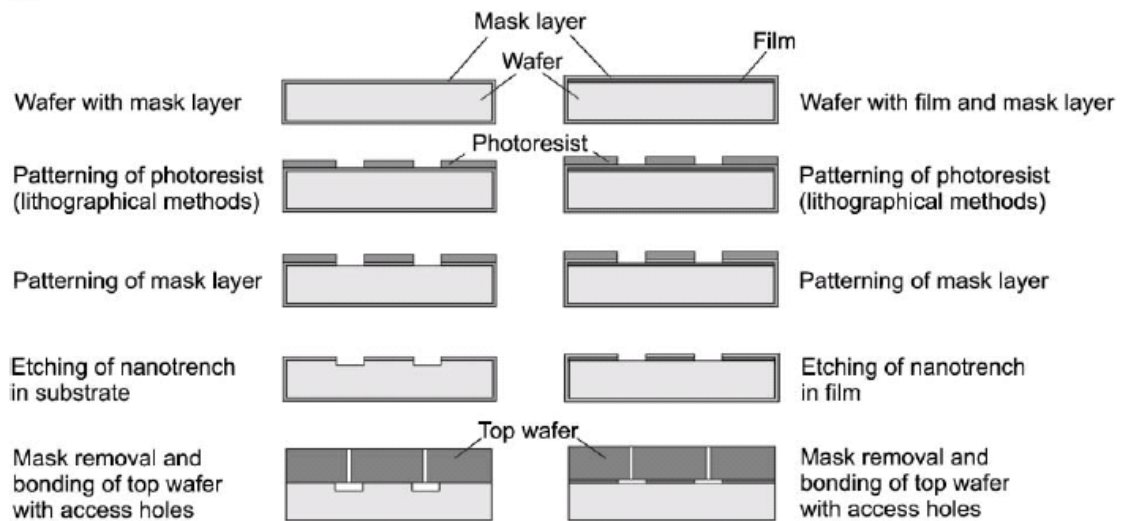


Figure 4 A typical lithography process to fabricate micro/nano-fluidic channel [27].

A typical process (cross section view) for fabricating micro/nano-fluidic channel using lithography techniques is shown in figure 4. Channel pattern is first transferred to substrate by photoresist and trenches are etched into substrate using photoresist as

masking materials. After removing the remaining photoresist, the substrate is finally bonded to a top cover wafer with fluid access holes permanently to form the channel. This technique is the most simple and common way to fabricate micro/nano-fluidic channel with high throughput [28, 29] and nanofluidic channel used this work is also fabricated with this method.

For conventional photolithography, the smallest feature one can print is around 500nm using I-line mercury lamp. If nanofluidic channel with width smaller than 500nm is needed, advanced lithography technique such as electron beam lithography (EBL) can be used. In this case, instead of UV exposure light, electron beam that has a much smaller wavelength than that of UV light (300-400nm) is used and EBL is typically capable of writing features on a 10-nm scale. In EBL, a focused beam of electrons is scanned over a resist, such as poly (methyl methacrylate) (PMMA), breaking bonds. The exposed areas are then selectively dissolved in a carefully selected organic solvent. Figure 5 shows one of nanofluidic channels fabricated by JBX-9300FS electron beam lithography system (JEOL Ltd., Tokyo, Japan) at Cornell Nanoscale Facility. The width of nanochannel is about 100nm. However, EBL is a serial process with very low throughput and high-cost. Besides the above-mentioned conventional bulk micro/nano-machining techniques, more sophisticated surface micro-machining (shadow deposition [30], sacrificial layer [31-33]), mold-machining (poly (dimethylsiloxane) (PMDS) [34, 35], nano-imprinting [36-38]), bottom-up self-assemble (co-axial electrospinning [39, 40], sacrificial electrospinning [41], flexible polymer tubes [42]) techniques are also

being developed. More complete overview of micro/nano-fluidic device fabrication techniques can be found in these references [27, 43-45].

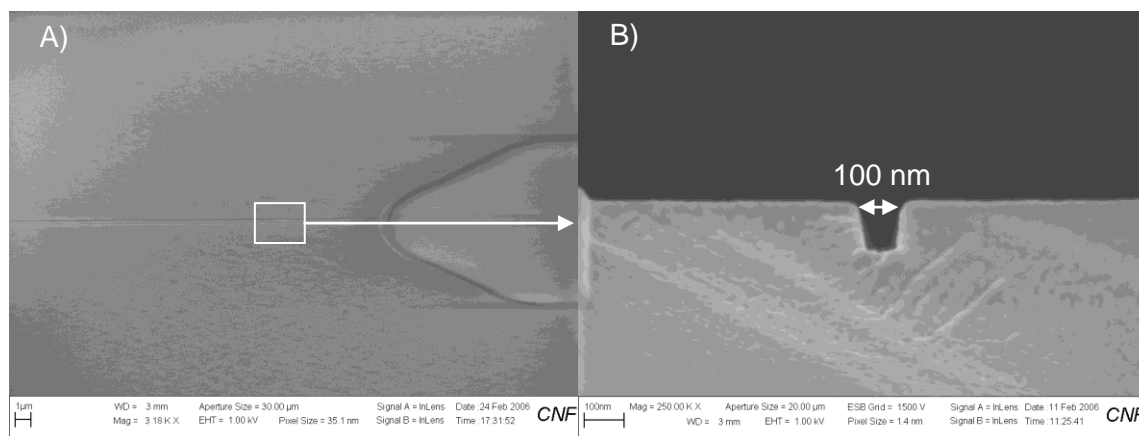


Figure 5 Scanning electron microscope (SEM) images of nanofluidic channel device. A) top view of EBL fabricated nanochannel. B) cross section view of the same nanochannel with width of ~100nm on fused silica substrate.

2.3 Micro/nano-fluidic single molecule detection

2.3.1 Technology overview

Using micro/nano-fluidic device as SMD platform are becoming more and more popular in recent years [14, 46-48]. Micro/nano-fluidic channel offers a spatial confinement of molecules in one or two dimensions in a continuous flow system. This will not only ensure a fixed position for interrogation of target molecules but also avoid repeated detection of the same molecule. As channel dimensions shrink and become comparable or smaller than the optical excitation volume, uniform excitation of target molecules and very high detection efficiency can be achieved. In addition, signal-to-noise ratio is improved significantly as the background from scattering or intrinsic

fluorescence of unlabelled species in the probe volume is minimized. To do SMD in bulk solution, normally low concentration of analyte is needed due to relatively large detection volume. But with the help of micro/nano-fluidic devices, it becomes possible to investigate molecules in their native environment or at their physiological concentrations, which are usually much higher, while still achieving single molecule resolution due to reduced probe volume. Furthermore, the implement of miniaturized devices greatly reduces sample consumption and as lab-on-a-chip technology advances, integrated high-throughput parallel detection system becomes feasible in the near future. By merging these two techniques, it is obvious that we can achieve the optimal requirements for the analysis and manipulation of biological samples on a single molecule level [46]. A number of applications can be found in recent literature, including DNA separation [49-51], sequencing [52], mapping and fragment sizing [31, 53-57], molecular conformation studies [58, 59], drug screening and chemical analysis [60, 61], microflow characterization [62], ultra-sensitive detection without target amplification [63], etc.

2.3.2 Molecule interaction study by micro/nano-fluidic SMD

Molecule-molecule interaction studies at single molecule level can be carried out in bulk solutions or on planer surfaces with specially-designed devices or sophisticated optical systems [64-70]. In this work, our focus is to apply micro/nano-fluidic SMD technique to study molecule interaction and in literature, studies of molecule interactions

in a microfluidic flowing environment [28, 71-74] have been reported in recent years. The following is a short summary of some of the related works.

Stavis and co-workers demonstrated efficient two-color fluorescence detection and characterization of Qdot 655 Streptavidin Conjugates binding to Alexa Fluor 488 molecules in a submicrometer fluidic channel [28]. Zhang and co-workers introduced a homogenous technique for rapid and sensitive probing specific DNA molecules using two-color quantum dots based on single-molecule coincidence detection in a capillary with inner diameter of 50 μm [74]. Most recently, Agrawal and co-workers reported the use of bioconjugated nanoparticles and two-color fluorescence coincidence for real-time detection of single genes, proteins and intact viruses in a flowing fused silica capillary with inner diameter of 2 μm [72].

All of the above works are detecting two molecule interactions with two colors and it's still a challenge to study interactions between three or more molecules. Our approach in this work would allow us to study up to four molecule interaction with only two colors. It could potentially revolutionize the field of molecular interaction.

2.4 Conventional protein detection and interaction study in cancer cell

2.4.1 Importance of protein interaction study in cancer research

In this section, an example of protein interaction study along one of the tumor signal pathways in breast cancer cell based on conventional assay is described to show the importance of this research and limitation of current assays. Over-expression of HER2 in breast cancer gives an increase to autophosphorylate itself and activates PI3K

through assembling the HER2/PI3K complexes. These complexes localize at membrane and convert PIP2 into PIP3 that serves as the second messenger to facilitate the activation of AKT. Phosphorylated and activated AKT mediates the activation and inhibition of several targets, resulting in great influence in cellular growth, survival and proliferation through various mechanisms. Among the downstream substrates of AKT, MDM2 is a critical modulator in regulating the tumor-suppressor protein p53 [5]. P53 is a transcription factor that can induce either growth arrest or apoptosis and is frequently mutated or deleted in many types of tumor [75-77]. In addition, many tumors with a wild-type gene for p53 do not have functional p53 protein, suggesting that some oncogenic signals suppress the function of p53 [75, 77]. The levels and activity of p53 are controlled largely by MDM2, which is amplified or over-expressed in a variety of human tumors and can function as an oncogene in tissue culture systems [6, 75]. MDM2 can bind directly to p53 and promote its ubiquitination and subsequently its degradation by the proteasome [6, 7]. The ability of MDM2 to degrade p53 depends on its ubiquitin E3 ligase activity and its nuclear localization signal and nuclear export signal, which are required for MDM2 to shuttle between the nucleus and the cytoplasm [6, 75]. The nucleus–cytoplasm shuttling of MDM2 presumably mediates p53 degradation by cytoplasmic proteasomes. Interestingly, we have revealed that HER2-mediated resistance to DNA-damaging agents requires the activation of AKT, which enhances MDM2-mediated ubiquitination and degradation of p53. AKT interacts physically with MDM2 and phosphorylates it at Ser166 and Ser186, and so increases the nuclear localization of MDM2. Furthermore, phosphorylation of MDM2 increases its interaction

with p300 and inhibits its interaction with ARF and so increases p53 degradation (figure 6) [5].

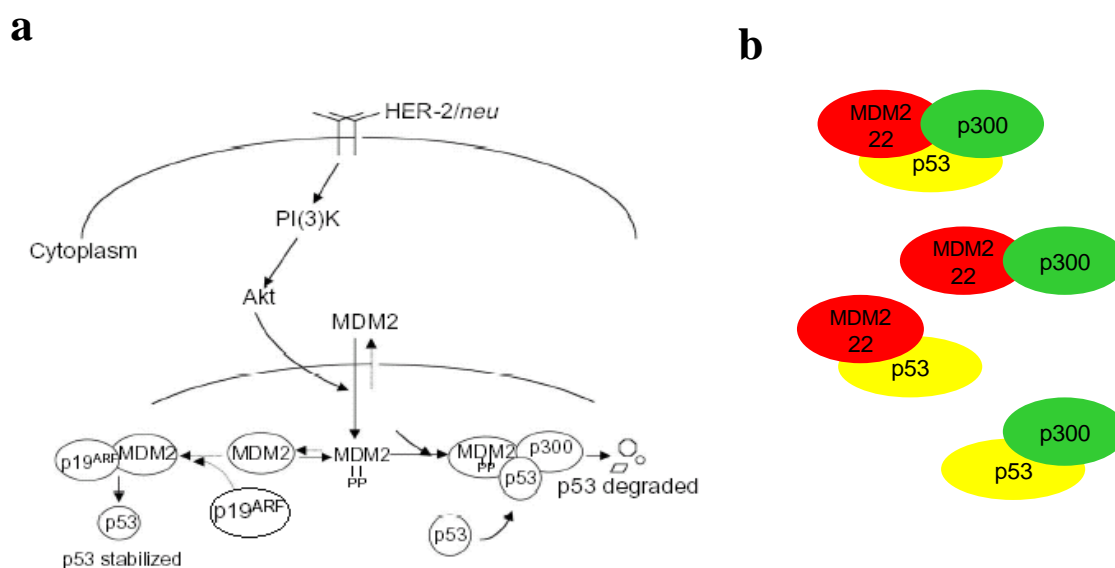


Figure 6 Protein interaction study along one of the tumor signal pathways in breast cancer cell. (a) A model showing how HER2 induces the nuclear localization and altered binding of MDM2 with p300 and ARF via AKT. (b) The possible different complexes combination in AKT-MDM2 signal pathway during analysis [5].

The identification of this pathway is important for understanding the role of AKT in p53 regulation in breast cancer and these finding was also been confirmed in clinical samples. However, we are still missing the information of the dynamic interactions within this pathway, which is important for us to clarify the causal relationship precisely. For instance, we would like to know whether the ARF bound MDM2 could still be phosphorylated by AKT and causing the dissociation of this ARF-MDM2 complex. And if the ARF-MDM2-AKT tri-complex exists, what are the population ratios in different

proteins combination complexes? Similar questions could also be applied on the MDM2-p300-p53 complexes (figure 6b). However, these questions are difficult to answer using current techniques. In fact, like many other breast cancer signal pathways research, scientists are facing similar difficulties when they need to address questions about the interaction and dynamics of multi-protein complexes. In this study, we used identified various breast cancer signal pathways as proof-of-principle experiments and develop this nanofluidic SMD technique for unknown molecule interaction study and further cancer signal transduction analysis.

2.4.2 Conventional protein detection and interaction assays

Currently, the most common assay for a molecular biologist to detect proteins and their interactions are called immunoprecipitation IP (protein identification) and co-immunoprecipitation (Co-IP) (protein interaction), which are subsequently followed by western blot to identify protein or interaction. Figure 7 is a simple illustration of a typical IP process. This technique involves using an antibody that is known to specifically binding to the target protein in a solution containing many other proteins. The antibody used in IP is normally coupled to solid-phase support, usually antibody-coated-beads with micrometer sizes, to facilitate the precipitation process. After centrifuge, target protein is pulled down by the antibody with the bead to isolate and concentrate from many thousands of different proteins in the solution.

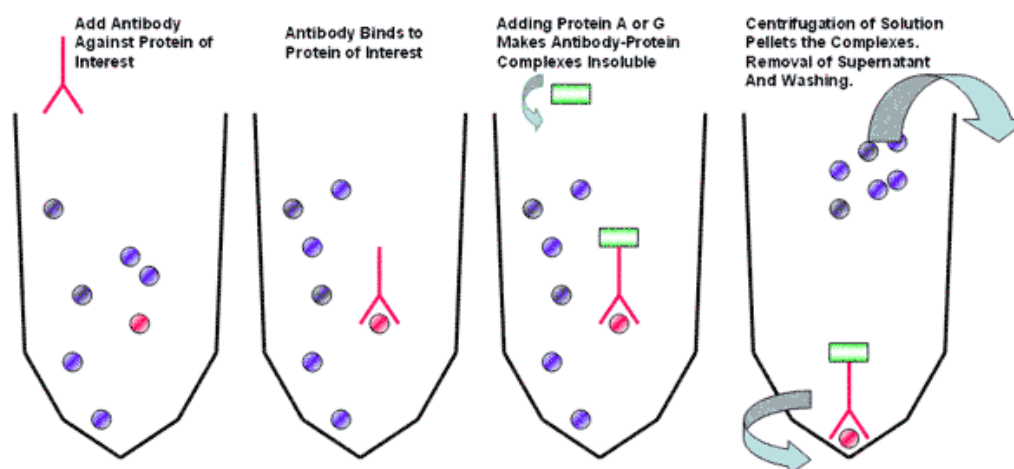


Figure 7 Illustration of a typical immunoprecipitation (IP) process [78].

For Co-IP, instead of single protein molecule, complex with two or more protein is being pulled down by antibody that is known to bind to one of the proteins in the complex. Western blot is then used to analyze the pulled-down protein complex to identify individual protein components in the complex and characterize the interaction, if there is any. Speaking of western blot, it is also called immunoblot, one of the popular analytical techniques used to detect specific protein in a given sample of protein extract. More specifically, gel electrophoresis is performed on the protein extract from Co-IP and different proteins are separated based on their lengths of polypeptides at different positions of the gel column. In the end, antibodies targeting specific protein are introduced into the gel column to verify the existence or absence of specific protein and compare their relative concentration.

Table 2 compares the most commonly used protein interaction assay with the micro/nano-fluidic SMD technique being developed in this work. To summarize, Co-IP/western blot has the drawbacks of long processing time, limited sensitivity, very

challenging for interaction study between more than two proteins, difficult to quantify interaction dynamics, etc. The micro/nano-fluidic SMD technique described in this work can potentially overcome these drawbacks and shed new light on the dynamics of some of the complex protein interactions along the tumor signal pathways in breast cancer cell.

Table 2. Comparison of Co-IP/western blot and micro/nano-fluidic SMD techniques for protein interaction study.

	Co-IP/western blot	Micro/nano-fluidic SMD
Signal Source	Ensemble of molecules	Single molecule
Sensitivity	Low	High
Processing Time	3 days	2-3 minutes
Sample Consumption	1 milligram	10 microgram
Quantification of Interaction Dynamics	No	Yes
Multi-protein Interaction	Limited to interactions between 2 proteins	Up to 4 proteins with two-color system Up to 6 protein with three-color system

3. MICRO/NANO-FLUIDIC CHANNEL FABRICATION

3.1 Bulk fabrication of fused silica micro/nano-fluidic channel








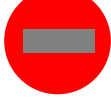

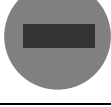

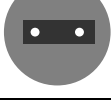

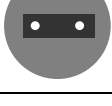
The micro/nano-fluidic devices used in this study were fabricated by standard photolithography, plasma etching and fusion bonding process at Cornell Nanoscale Facility (CNF), which is a national user facility that provides state-of-the-art micro/nano-fabrication tools coupled with expert staff support. Bulk micromachining is one of the simplest and most straight-forward microfabrication techniques to fabricate microfluidic devices. Table 3 provides a typical bulk microfabrication process used in this study. Since our technique is fluorescence-based and operating on an inverted microscope, transparent fused silica becomes our choice of substrate material. In addition, UV-grade fused silica must be used because the wavelength of our diode laser excitation source is 375nm, which is in the UV range. In this study, two channel designs are used. One has a width of 2 μ m at detection region fabricated by contact photolithography while the other has a width of 500nm at detection region fabricated by projection photolithography.

3.1.1 Contact lithography for 2 μ m-wide microchannel

As the name suggests, contact lithography brings mask plate to close proximity of the substrate and transfers pattern onto wafer at 1:1 ratio. 500 μ m-thick UV grade fused silica wafer (Mark Optics, Santa Ana, CA) is first coated with positive Shipley 1818 (Shipley Company, L.L.C., Marlborough, MA) photoresist. After a brief softbake

at 115 °C to drive out moisture in the photoresist, the wafer is inserted into the contact aligner (EV620, EV Group, Inc., Albany, NY) for exposure.

Table 3. Typical microfabrication process flow of microfluidic device used in this study.

Cross Section View	Top View	Process
		Double-side polished 4" fused silica wafer
		Spin coat photoresist on wafer
		Photolithography pattern the photoresist and develop
		RIE etching fused silica substrate to desired depth
		Removal of remaining photoresist
		Creating fluid access holes
		Fusion bonding of cover wafer to substrate wafer

The minimum feature we can achieve with this contact aligner is 2 μ m. The exposed wafer is then developed in AZ 300 MIF (MicroChem Corp., Newton, MA) for 1 minute and followed by 115 °C hardbake for 1 minute to increase photoresist's etch

resistance. CF_4 reactive ion etching (RIE) is performed to plasma etch a shallow trench into fused silica substrate. The reasons we chose to use CF_4 RIE for etching are as following: 1) square cross section etch profile; 2) smooth channel surface; 3) accurate control of etch depth. The wafer is then brought inside a parallel plate oxford plasma 80 etcher (Oxford Instruments, Oxfordshire, UK). CF_4 gas at 20 standard cubic centimeters per minute (SCCM) is feed through during RIE at a power of 150W under 20mTorr chamber pressure and trenches with depth of 500nm are etched into fused silica in about 25 minutes. Etching to a depth slightly less than the channel width resulted in some degree of automatic filtration to prevent clogs, often an issue in fluidic channels [28]. After etching, the remaining photoresist mask is removed by O_2 plasma. Figure 8 shows the optical image of microfluidic channel with width of $2\mu\text{m}$. The next step is to create fluid inlets and outlets. The substrate wafer is covered with a surface coating material called FSC-M (MicroChem Corp., Newton, MA) to protect the wafer and channel surface. Then the inlets and outlets are blasted through the substrate wafer by high-speed alumina power. After sand blasting process and removal of FSC-M coating, both the substrate and cover wafers are subjected to various thorough surface cleaning procedures, including hot piranha clean (3:1 mixture of concentrated sulfuric acid (H_2SO_4) with hydrogen peroxide (H_2O_2) at $70\text{ }^\circ\text{C}$ to remove any organic traces), to insure an extremely clean and particle-free fused silica surface, which is very critical for the final bonding process. Cover fused silica wafer of $170\mu\text{m}$ -thick is chosen because the inverted microscope we use is equipped with a 60x water immersion objective with a maximum working distance of $200\mu\text{m}$.

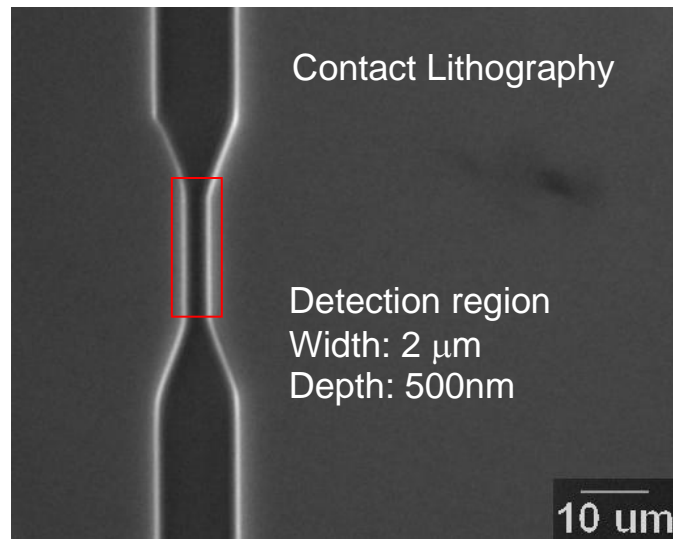


Figure 8 Optical image of microfluidic channel with width of 2 μ m.

A water fused silica bonding process is developed based on reference 79 and it takes advantage of dehydration and condensation/polymerization of Si-OH groups on fused silica surface that is being covered with water to form temporary Si-O-Si bond at the interface [79]. For actually bonding procedure, first cover both substrate and cover wafer with a layer of de-ionized (DI) water and then bring two wafers in contact and let the water evaporates under a laminar flow hood. In this way, the quality of the initial bonding is much better than the method described in [28], which place two wafers in contact without an intermediate water layer. Finally, a high temperature treatment must be performed to achieve a permanent bonding or hermetic seal of substrate trenches. Fused silica has a melting temperature of 1723 $^{\circ}$ C, but it will start softening around 1100 $^{\circ}$ C and form permanent Si-O-Si bond at the interface. Therefore, we perform the fusion bonding process at 1100 $^{\circ}$ C in a regular air furnace for 7 hours to complete the

device fabrication. Figure 9 shows a photo of microchannel device after fusion bonding. In the end, solution reservoirs are attached to the inlets and outlets by using 5-minute epoxy.

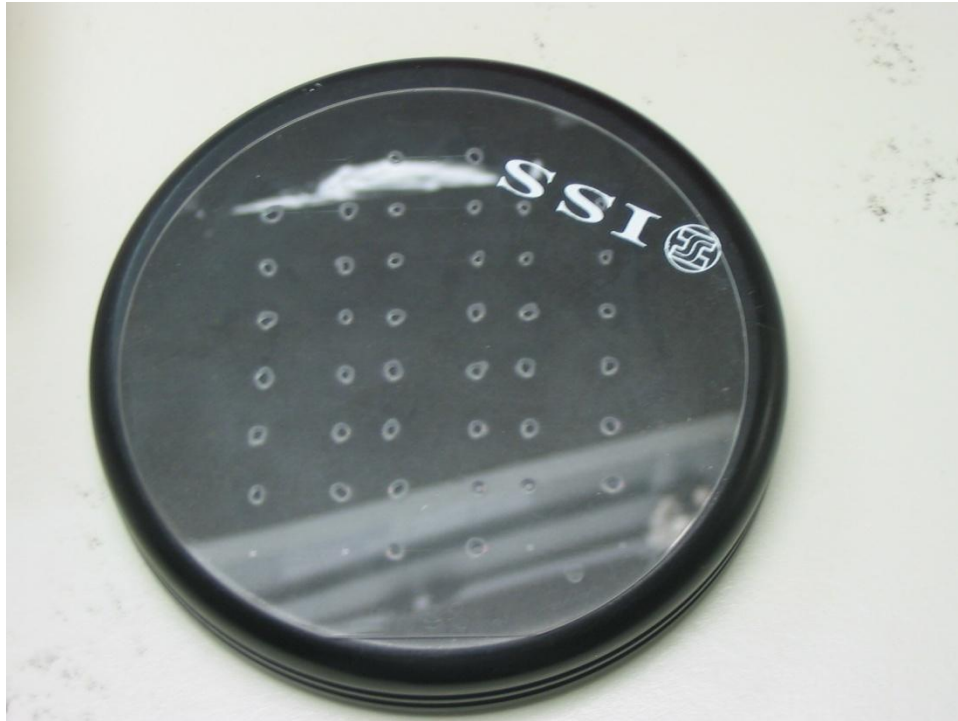


Figure 9 Photo of a microchannel device after bonding.

3.1.2 Projection lithography for 500nm-wide nanochannel

Decrease in the optical detection volume will lead to increase in signal-to-noise ratio and more uniform excitation, as stated in previous section. One way to achieve this is to reduce channel dimension, in other words, fabricate smaller micro/nano-fluidic channels. With this in mind, we turned to projection lithography to fabricate channels with width smaller than $2\mu\text{m}$. In contact lithography, photomask covers the entire

substrate wafer and prints pattern at 1:1 ratio. However, for projection lithography, a condenser lens is placed in between UV source and mask plate. Pattern is being printed at 5:1 or 10:1 reduction ratio on only a small part (“die”) of the substrate. With this technique, we are able to print feature as small as 500nm using a GCA Autostep 200 DSW I-line Wafer Stepper. The focus system of this tool uses broadband light, which is idea for transparent substrate, such as fused silica. Before patterning real devices, an exposure dose test needs to be performed to determine the optimal exposure time and focus. Figure 10 shows a SEM image of nanofluidic device with width of 500nm fabricated by projection lithography. The general fabrication process is similar to that of contact lithography for 2 μ m-wide channel and detailed step-by-step process flow can be found in Appendix A.

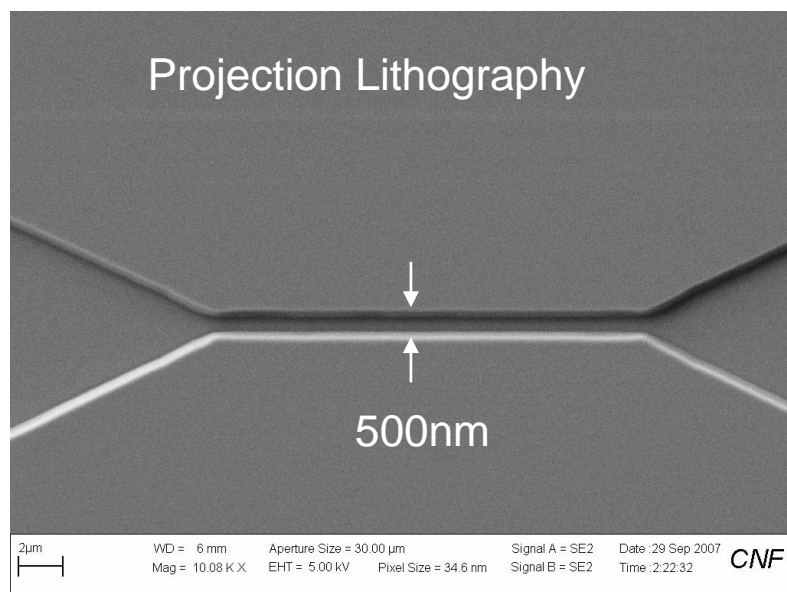


Figure 10 SEM image of nanofluidic channel with width of 500nm.

3.2 Surface modification of fused silica channel

When fused silica is in contact with an aqueous solution, its surface hydrolyzes to form silanol surface group [80]. For a solution with PH of 7, the surface group is negatively charged Si-O^- . Unfortunately, most proteins are positively charged at PH around 7. For this reason, protein molecules are known to stick to fused silica surface due to strong electrostatic interaction and the phenomenon is even worse in microfluidic channel, which has a high surface-to-volume ratio. This presents significant challenge for protein study in fused silica micro/nano-fluidic environment. In fact, severe protein adsorption is observed near the inlet of bare fused silica microchannel. In this case, Quantum Dot 525 (QD525) conjugated goat anti-rabbit antibody is introduced into the microchannel. Very strong fluorescence signal from QD525 is detected near the entrance of the microchannel and intensity decrease dramatically as it moves towards outlet of the microchannel, as shown in Figure 11. Almost no fluorescence signal can be detected in the middle part of the microchannel, where the detection region is. It suggested that QD525 antibody conjugates are severely adsorbed to the surface of fused silica and most of QD525 is lost to the channel wall. It is obvious that an effective way to prevent or minimize protein adsorption needs to be developed for this technique to work.

Various fused silica surface coating schemes have been developed this purpose [81]. High-molecular-mass polyethyleneimine (PEI) coating was introduced by Bedia Erim and co-workers for separation of basic proteins and peptides by capillary electrophoresis [82]. PEI is a positively charged polymer and found to absorb

irreversibly to the fused silica surface and forms very stable cationic static absorbed coating, even after flushing with strong acid or base [81].

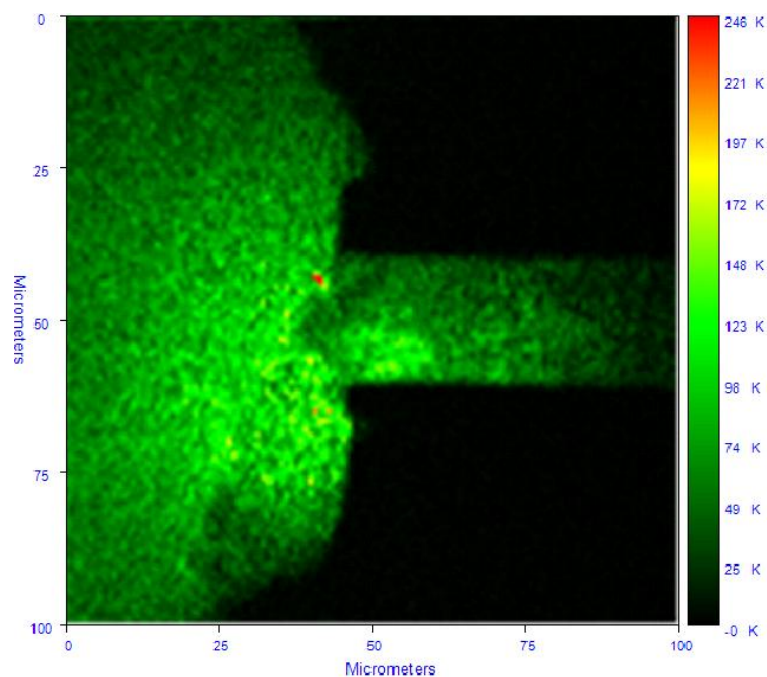


Figure 11 Fluorescence image of bare fused silica microchannel filled with QD525. Image is taken near the inlet.

In this study, coating solution containing 0.5% (w/v) PEI ($M_w=50,000-100,000$, Alfa Aesar, Ward Hill, MA) in IP buffer is prepared. The coating procedure is simply capillary filled the channel with PEI-IP buffer and let it sit for overnight. To confirm this coating method is effective, we compare the autocorrelation data of QD525 in channel under 100V, as shown in figure 12. With same QD525 solution, surface coated channel recorded much more events than uncoated channel, in other words, detection efficiency is significantly improved after surface coating.

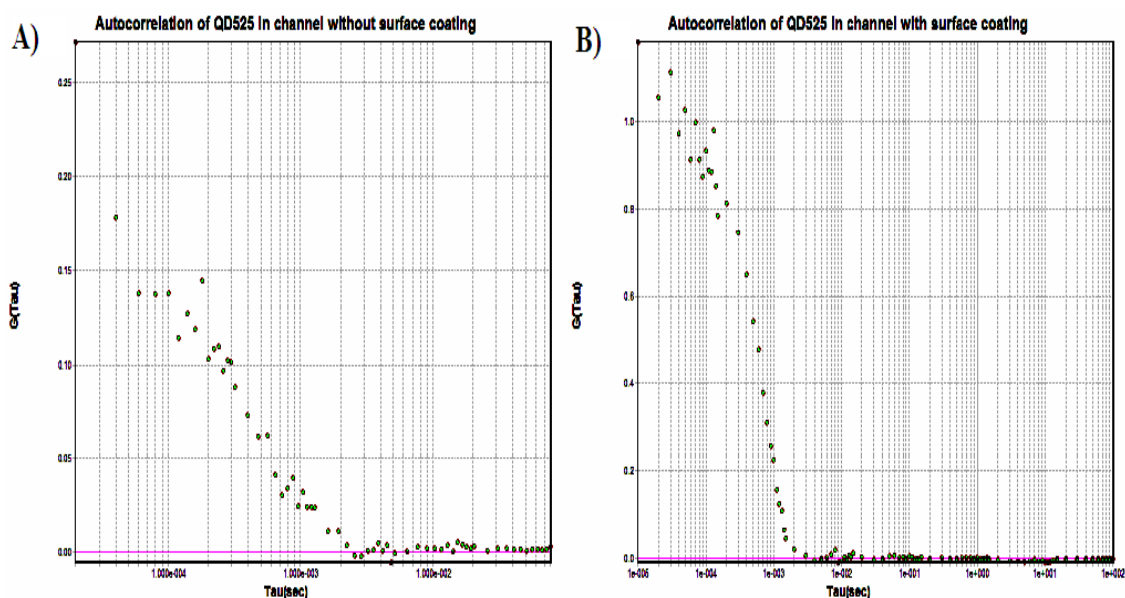


Figure 12 Autocorrelation of QD525 in microchannel under 100V. A) channel without PEI coating; B) channel after PEI coating.

Since PEI coating is to neutralize the negative surface charges, another way to verify the effectiveness of PEI coating is QD525 flow direction under external electric field. There are mainly two forces acting on a charged particle in microfluidic channel under external electric field. One is called electroosmotic force, which is originated from the electric double layer formed near the channel surface. Often it is also called electro-osmotic flow (EOF). For example, in figure 13A, the positively charged ions are attracted to negatively charged surface and accumulated near channel wall. Under external field, these clustered positive ions move towards the negative electrode and at the same time, it drags the rest of the solution with them. Another force is the electrophoretic force. It is simply that the positively charged ions will move towards the negative electrode. In terms of magnitude, electro-osmotic force is usually dominant

over electrophoretic force. Protein molecules are normally positively charged under our experiment conditions, therefore both of the EOF and electrophoretic forces are pulling proteins towards the negative electrode for a bare fused silica microfluidic channel. However, if the channel surface is coated with PEI, situation could be different. As a matter of fact, we observe Qdots almost exclusively move towards positive electrodes in PEI-coated channel, which is just the opposite of the situation in bare fused silica channel. This could only suggest a positively charged channel surface resulting from PEI coating, which induces an electro-osmotic flow towards positive electrode, as shown in Figure 13B. Therefore, the flow direction of Qdots in PEI-coated channel also indicates a successful surface modification by PEI coating solution.

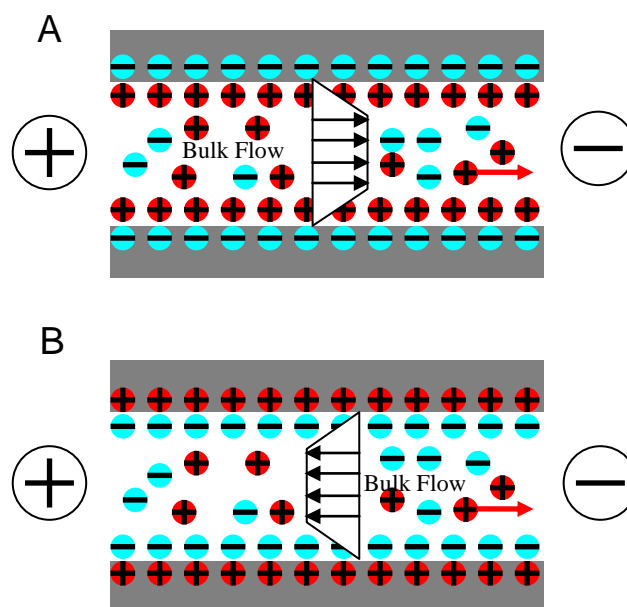


Figure 13 Electro-kinetic bulk flow inside fused silica channel (pH~7). A) Bare fused silica channel; B) fused silica channel coated with PEI. Red arrows indicate the direction of electrophoretic force under external electric field.

4. MATERIALS

4.1 Quantum dots

The fluorescence label we choose for our fluorescence SMD experiment is quantum dot, also called semiconductor nanocrystal. It's an inorganic nano-sized particle that emits fluorescence upon optical excitation and the wavelengths of the emission are controlled by the size of the semiconductor nanocrystals due to its quantum confinement properties [83-85]. Over the last two decades, significant progress has been achieved in terms of understanding, fabrication, functionalization and application of Qdots. Commercial water-soluble biological functionalized Qdots are available in different colors from Invitrogen, Inc. Figure 14 illustrates the structure of Qdots. The most popular Qdot is the semiconductor CdSe/ZnS with CdSe being the core and ZnS being the shell, as shown in the figure 14. The higher bandgap ZnS shell provides the necessary confinement for the CdSe core.

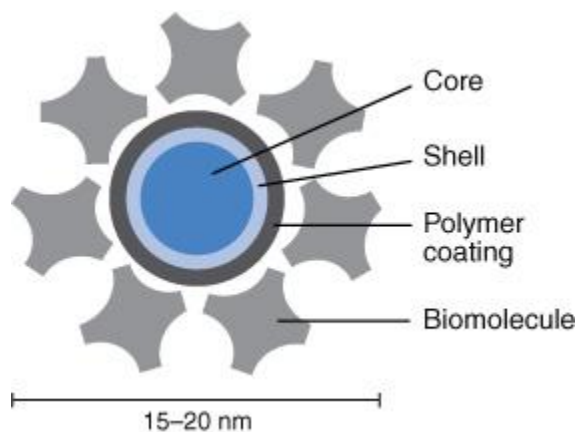


Figure 14 Structure of functionalized Qdot [86].

The purpose of polymer coating and outmost biomolecule is usually to make the inorganic Qdots water soluble and functionalized for specific biological applications. The unique property of Qdots is the wavelengths of their fluorescent emission are controlled by their sizes and the emission spectrum is very narrow, as shown in figure 15. Qdots with peak emission at 525nm, 605nm and 655nm are named as QD525, QD605 and QD655 in this study.

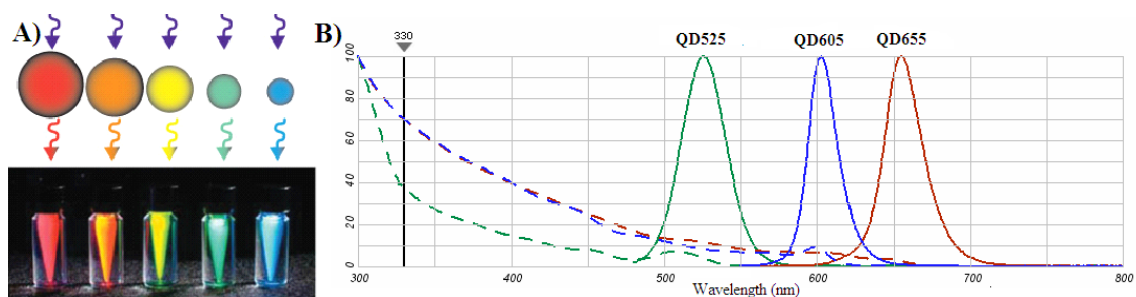


Figure 15 Size dependable emission spectrum of Qdot. A) Emission red-shift for larger Qdots; B) Emission spectrum of QD525, QD605 and QD655 [86].

For our application, the reasons we chose Qdots over conventional organic dyes are as following: 1) Very high quantum yield and superb brightness of Qdots. SMD experiment often suffers from low signal-to-noise ratio and the superb brightness of Qdot could definitely improve the signal-to-noise in this aspect. 2) Organic dyes under long-time excitation could lose its fluorescence capability due to oxidation process and result in reduced emission or irreversible damage. This process is also called “photobleaching”. However, since Qdots are inorganic, they have exceptional photochemical stability; in other words, they don’t usually photobleach even under long-

time excitation. 3) Conventional organic dyes usually have a broad emission spectrum, such as a long tail into red. As a result, spectral cross-talk poses potential problems for the multi-color detection scheme, which is implemented for our protein interaction study. Figure 15B shows very narrow emission bandwidth of Qdots and very little spectral overlap between QD525, QD605 and QD655. Therefore, Qdot is much better candidate for our multi-color detection in this respect. 4) Last but not least, Qdots also exhibit very broad adsorption spectrum, as shown in figure 15B. This means that with only one excitation source we could excite multiple Qdots with different colors at once. This not only would significantly lower the cost of our system, but also simplify the complexity of the system, as the setup of multiple excitation lasers are expensive and would need very accurate and complicated alignment.

4.2 Sample preparation

QD525 and QD605 conjugated goat anti rabbit or anti mouse antibodies (Invitrogen, Inc.) were used as secondary antibodies in our experiment. Before each use, Qdots is centrifuged at 5000rpm for 3 minutes to precipitate out any aggregation formed in solution. Various target protein solutions, including their corresponding primary antibody and secondary antibody/Qdot are prepared for detection. The following shows a typical sample preparation protocol. The target Hemagglutinin (HA) epitope tagged MAX (HAMAX) cDNA was transfected and overexpressed in HEK293 cell line. The cells were then lysed by RIPA lysis buffer and total cell lysates were collected to measure the protein concentration before subsequent analysis. 500 μ g of protein lysate

sample was diluted in IP binding buffer (20mM Hepes-KOH, 0.1mM KCl, 2mM MgCl₂, 15mM NaCl, 0.2mM EDTA, 1mM DTT, 10% glycerol) at PH around 7.5 and made it to final total 1ml. 5µl of rabbit anti-HA tag primarily polyclonal antibody (Santa Cruz, 200mg/ml) was then added into the sample and rotated in 4 °C for overnight. Subsequently, 2µl of QD525 conjugated anti-rabbit antibody (1µM) was added into the sample and incubated in room temperature for 1 hour and then diluted 10 times in IP binding buffer. The sample is then ready to be loaded into the channel for detection. Similar sample preparation protocol applies for other target protein detection or protein interaction experiments.

5. FLUORESCENCE SMD IN FLUIDIC CHANNEL

5.1 Experiment set-up

A commercial fluorescence correlation spectrometer system is implemented for our SMD experiments, as shown in figure 16. The system consists of three major parts, including laser launcher module (right in figure 16), inverted microscope (middle in figure 16) and dual channel detection system (left in figure 16).

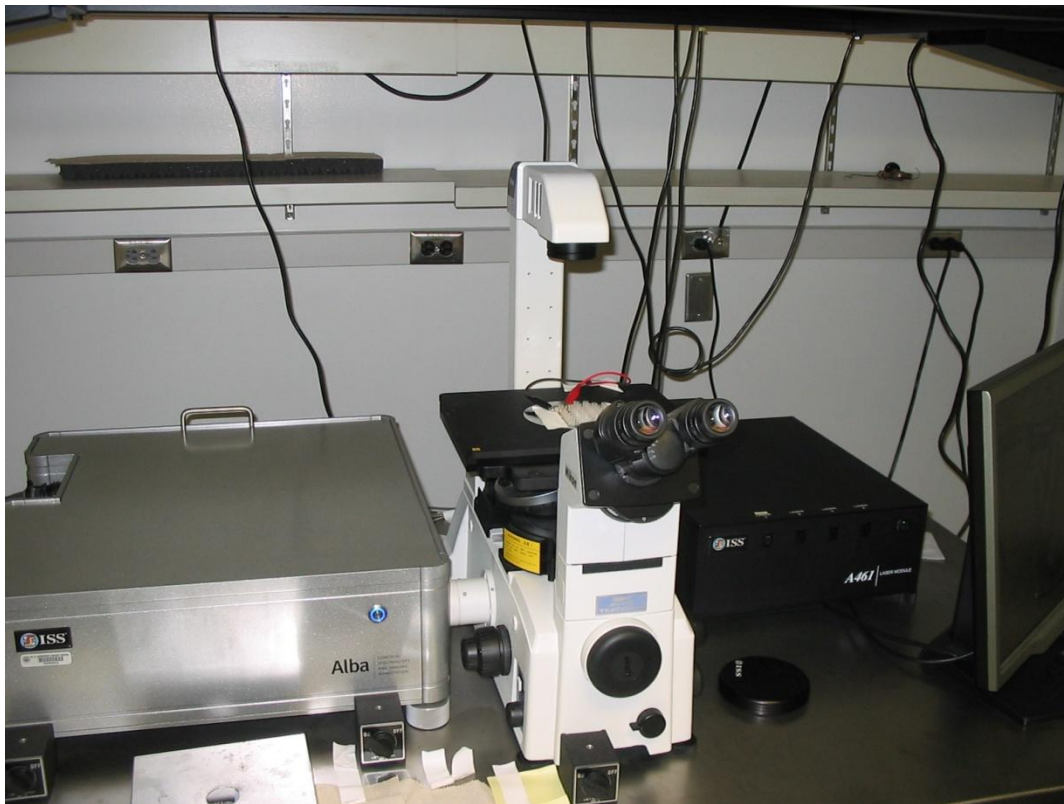


Figure 16 Photo of fluorescence correlation spectrometer system.

A 375nm diode laser is chosen as excitation due to reasonable good adsorption of QD525, QD605 and QD655 at this wavelength. The diode laser is installed inside the laser launcher module and a fiber optical cable connected in the back from the module to microscope is used to feed the laser into the microscope. The optical path and detailed configuration parameters of the system are shown in figure 17. Laser is focused into channel by an inverted Nikon TE2000 microscope with 60x water immersion objective, which has a numerical aperture (N.A.) of 1.2. Higher the N.A., smaller the beam spot, thus higher the signal-to-noise ratio. The maximum working distance of this water immersion objective is 200 μm , therefore, cover wafer with thickness less than 200 μm must be used. An average laser power of 20 μW is measured at the objective.

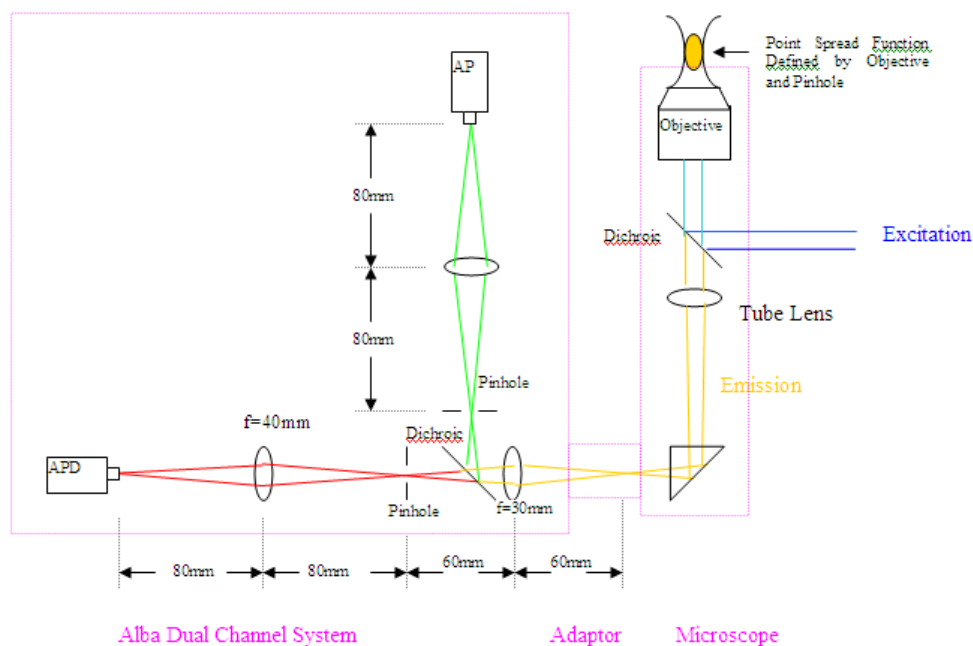


Figure 17 Optical path of fluorescence correlation spectrometer system and detailed configuration parameters.

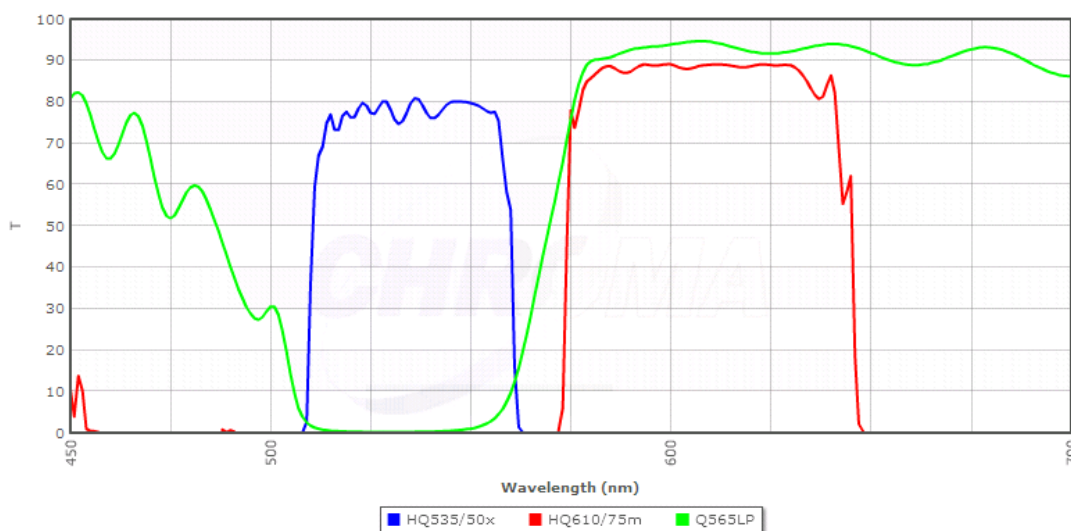


Figure 18 Transmission spectra of dichroic mirror and filter set implemented in dual channel system [87]. Green is the long-pass dichroic mirror, blue is the band-pass green filter, red is the band-pass red filter.

Fluorescence emission from the Qdots is fed into the dual channel detection system through an adaptor connected to the microscope. A dichroic mirror (inside dual channel system in figure 17) has a transmission spectrum (green) showing in figure 18. It allows transmission of red light and longer wavelength light into one detector and reflects green light to the other detector. Before each detector, a green band-pass filter is placed for green channel while a red band-pass filter is placed for red channel. Their spectrums are shown in figure 18 as well. To further restrict the detection volume, 50 μm -diameter confocal pinholes are also implemented for each channel. As for photon detector, the system equips two silicon avalanche photodiodes (APD) from PerkinElmer, Inc. The module SPCM-AQR-15 is capable of detecting single photons of light over the 400nm to 1060nm wavelength range. It has an active detecting area of 175 μm in

diameter with a dark count of <50 counts/second. To collect and analyze photon signals from APD, a data acquisition card capable of performing real-time FCS analysis and dual channel raw data storage is connected to the output of APD. Real-time results, including FCS and counts per second (CPS), are displayed with FCS software on a personal computer.

5.2 Experiment procedure

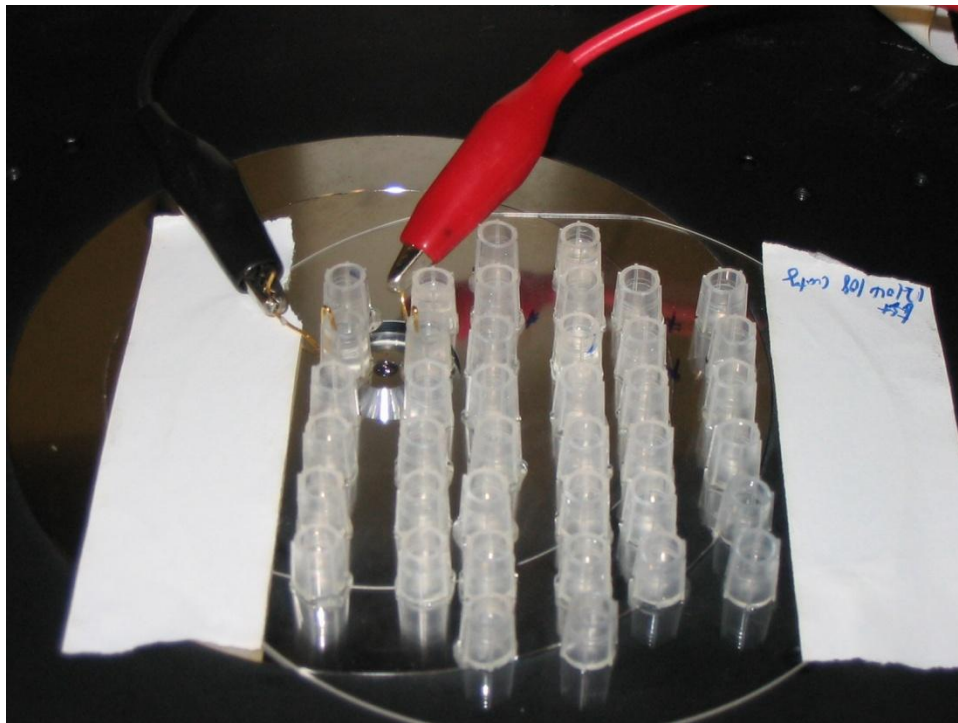


Figure 19 Photo of microchannel device on microscope stage during detection. Gold wire electrodes inside the solution reservoirs are connected to a high voltage power supply providing external electric field.

In the nanofluidic regime, because of its small dimensions, the flow resistance is so high that hydro-dynamically driving aqueous solution through channel becomes very challenging due to unrealistically high pressure needed. Therefore, for our application, instead of hydro-dynamically, we electro-kinetically drive the solution through the channel with an external electric field. As discussed in section 3, for aqueous solution, an electrical double layer forms near the surface of fused silica. Clustered counter-ions near the surface move under external electric field and drag the entire liquid body move in the same direction. Depending on the magnitude of the electric field, flow velocity can be adjusted. Figure 19 shows a photo microchannel device on microscope stage during detection. First, using binocular, the water immersion objective lens is carefully focused and aligned to the detection region of the nano/micro-fluidic channel. Then the device is taped on the stage to avoid movement during detection. Two gold wires are inserted into the solution inlets/outlets and used as electrodes due to their chemically inert properties. Two alligator clips connect the gold wires to a high voltage power supply (Model PS350, Stanford Research Systems, Inc.), which is capable of generating up to 5000 volts. In this study, sample solution in microchannel is electro-kinetically driven at various potentials up to 500V. During detection, all room lights are turned off to avoid any interference from ambient and commercial FCS software is used to monitor real-time signals, including correlation and CPS, and acquire data. Since the objective lens we are using has a limited depth of focus, we need to adjust the laser focus before acquiring any data. In order to be consistent for each measurement, we always adjust the focus to the point where CPS is maximized. As for data acquisition, there are two modes

with the FCS software. One is called *time* mode and the other is *photon* mode. In time mode, the number of photons collected within a specified time interval is counted. The extension of the time interval is determined by the frequency of the sampling frequency specified by the user through the software. Time intervals are selectable, from as short as 20ns (50 MHz) to as long as 1.3ms (763 Hz). If the phenomenon under investigation occurs in a short time scale, one may need to utilize time intervals of the order of 1 μ s or shorter; conversely, for processes that occur on a longer time scale, the duration of the time intervals will be longer. In photon mode, the acquisition card records the time delay between one photon and the next photon arriving to the detector. In this implementation of the data acquisition, the number of clock cycles is the event to be recorded and the photons are the start-stops defining the interval. Photon mode data acquisition provides and contains information on the photon stream arrival. The information can always be transferred to time mode at any frequency lower or equal to the inverse of the time clock. Therefore, the photon mode data file contains more information than the time mode data file and (a) allows obtaining information on very short times processes without producing large data files and, (b) it is very advisable for measurements with low counts per seconds. Based on the applied voltage range and channel dimension in this study, most of SMD target events happen in a time scale of milliseconds. As a result, we choose time mode for our data acquisition and a sampling frequency of 10 μ s (100kHz). Each measurement is 50 seconds, which corresponds to 5 million points at 100kHz frequency. At the end of each measurement, time mode raw data in ASCII format are recorded for further data analysis.

5.3 Data analysis

5.3.1 Fluorescence correlation spectroscopy (FCS)

FCS is an experimental technique, which applies time-averaging statistical analysis on the fluctuations of fluorescence intensity, which result from fluorescent molecules entering and leaving the sample observation volume [88-90]. It combines maximum sensitivity with high statistical confidence, which enable analysis at single molecule level [91]. In general, all physical parameters that give rise to fluctuations in the fluorescence signal are accessible by FCS [92]. For example, information on local molecule concentration, mobility, conformational fluctuations, characteristic rate constants of inter- or intra-molecular reactions, etc. can be obtained with this technique [92]. Although FCS is not the focus of data analysis in this study, we do perform FCS to obtain parameters such as mobility/residence time of each molecule in the detection volume and monitor the process in real time during each measurement. Therefore, a brief introduction of FCS technique is presented in this section.

On the mathematical side, correlation simply refers to multiplying one signal by a delayed version of a second signal and integrating or time-averaging the product. There are two types of correlations depending on the source of the second signal. One is called autocorrelation, where the second signal is just the first signal itself. A temporal analysis of average fluctuations δF in the recorded fluorescence signal $F(t)$ is carried out by temporal autocorrelation of $F(t)$, giving rise to a normalized fluctuation autocorrelation function $G(\tau)$ showing in equation (1) [91],

$$G(\tau) = \frac{\langle \delta F(t) \delta F(t+\tau) \rangle}{\langle F(t) \rangle^2} \quad (1)$$

In other words, autocorrelation correlates with the same time signal to measure for the self-similarity and highlights characteristic time constants for underlying processes and the development of an autocorrelation curve is shown in figure 20 [92]. Based on specific experiment conditions, one can develop specific autocorrelation models [93]. Then you can fit the raw data with the mathematic model to obtain useful information, such as local concentration, diffusion constant and flow velocity, etc.

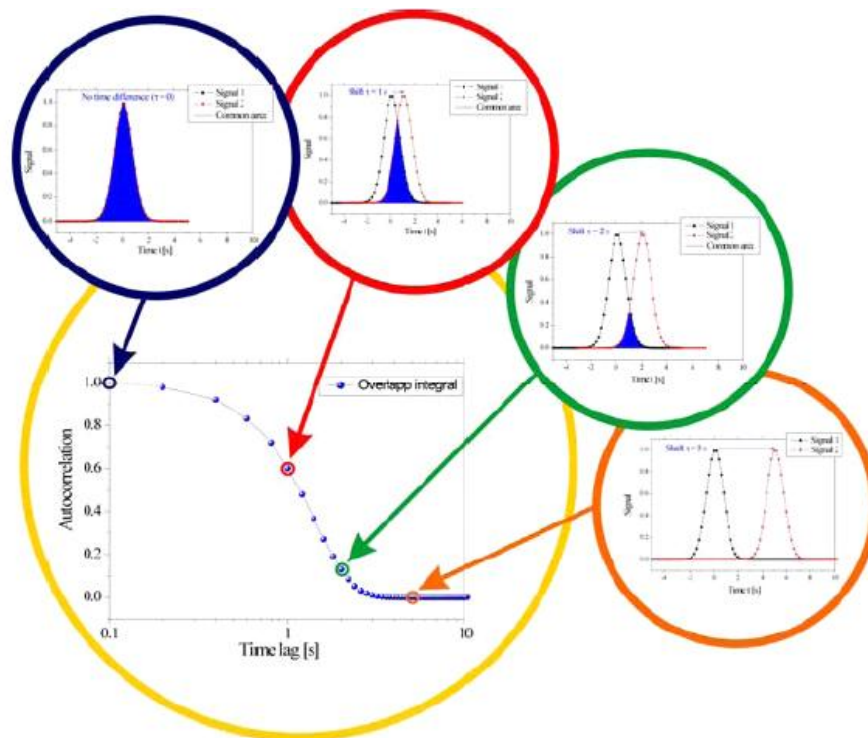


Figure 20 Development of an autocorrelation curve [92].

The other correlation method is called crosscorrelation, where in this case the second signal is different from the first signal. It correlates two independent time signals to measure common features of these two signals. This is especially useful for studying

molecule-molecule interactions. For example, one molecule is labeled with red fluorescent tag and the other molecule is labeled with green fluorescent tag. Crosscorrelation of two signals from red channel and green channel can be viewed as an indication of interactions between these two molecules, i.e. physical binding, if there is any. For our dual-color molecule interaction experiments, it is very helpful to monitor the real-time crosscorrelation as an indication of interaction events.

5.3.2 Two-dimensional (2D) photon burst analysis

One of the novelties of this study is the implementation of this 2D photon burst analysis on SMD data to detect target protein, measure relative concentration of target protein, and detect protein-protein interaction. More specifically, this 2D photon burst analysis is to collectively generate a burst diagram of photon counts versus burst widths of individual molecule events. Each plot could contain over hundreds or even thousands of single molecule events from a single measurement. This analysis could provide characteristic information of different molecules or molecule complex depending on their spatial locations on the 2D diagram, which could lead to identification of target protein or complex in a protein mixture while comparing to that of the control sample. Before one can plot 2D photon burst diagram, time mode raw data in the format of ASCII needs to be analyzed to identify individual molecule events. A threshold count is determined to distinguish noise from actual single molecule events. This threshold is usually defined as the mean background intensity plus three times the standard deviation for a particular measurement [46]. Assuming photon count signal follows Poissonian

distribution [61], the standard deviation is the square root of the mean background intensity. Once the threshold count is set, the raw data is processed and singled out all the identified events that are above the threshold. Then these events are analyzed individually. The total photon count and the duration of each event (total number of integration time) are recorded and plotted on the 2D photon burst diagram. Figure 21 illustrates the procedure of plotting the 2D photon burst diagram for one event. This process is repeated for each identified event for a particular measurement and a 2D photon burst diagram containing hundreds or thousands of events can be generated.

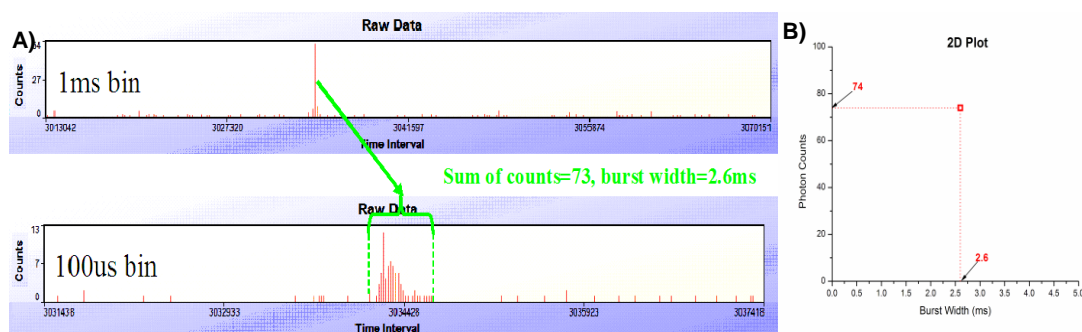


Figure 21 Procedure of plotting 2D photon burst diagram. A) Calculating photon counts and burst width for a particular event; B) Corresponding event from A) plotted in a 2D photon burst diagram.

More often than not, one event could consist more than one integration time and ideally, every event consists of a gradual increase and decrease of photon counts [94]. However, Poissonian fluctuations lead to the possibility that the number of photon counts can be below a chosen threshold even after the beginning or before the end of an event [94]. As a result, one actual single molecule event could be identified as several

smaller separate events, which will lead to underestimate of burst width and photon counts and large increase in number of events of low burst size. To minimize this effect, before further analysis, a moving average method is applied in order to “smooth” the raw data to preclude a distortion of the burst size distribution when applying a simple threshold procedure [94]. From statistic point of view, moving average is simply creating an average of one subset of the full data set at a time with each number in the subset given an equal statistical weight. Given a data set $\{a_i\}_{i=1}^N$, an n-window moving average is a new data set $\{a_i\}_{i=1}^{N-n+1}$ obtained from the a_i by averaging the following n terms showing in equation 2,

$$s_i = \frac{1}{n} \sum_{j=1}^{i+n-1} a_j \quad (2)$$

The size of the subset, or moving window, is determined based on how fast Qdots move through the focal volume. For the time series photon burst raw data in our experiments, the window of moving average is set to be the number of time bins that is corresponding to the residence time of Qdots in detection volume. Figure 22A shows an example of an actual burst event and Poissonian fluctuations lead to photon counts drop below the threshold within the burst. After performing moving average on the same burst signal, photon counts becomes a gradual increase and decrease signal, as shown in figure 22B. For all the 2D photon burst analysis in this study, moving average method is performed on all the raw data before further analysis. Due to large number of events for each measurement, a self-developed MATLAB™ code is used to perform all the operations

described above to obtain the photon counts and burst widths of individual events and generate 2D photon burst diagram.

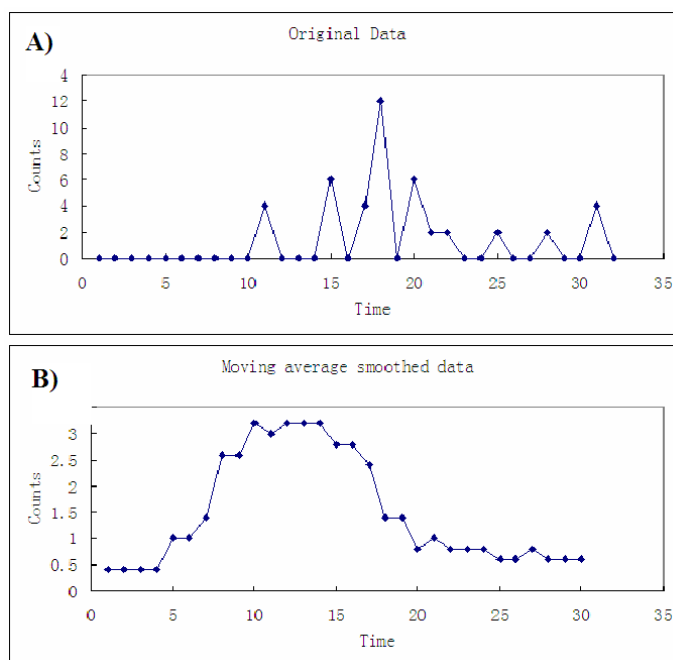


Figure 22 Effect of moving average method on photon burst signal. A) An actual photon burst signal; B) same burst after moving average operation

5.3.3 Dual-color photon burst coincidence analysis

In addition to the one-color 2D photon burst analysis described in the previous section, we introduce a dual-color photon burst coincidence analysis technique, which could in principle enable us to quantify the dynamics of the interaction between up to four proteins. Figure 23 shows the schematics of the principle behind the dual-color photon burst coincidence analysis. In this case, QD525 and QD605 are both present in the sample. Events from both channels are analyzed at the same time for a particular

measurement in the similar way described in the previous section. However, instead of photon counts vs. burst width for one color analysis, we plot all the events in terms of their red channel and green channel photon counts, as shown in figure 23. For an example, the green channel photon count value of a red channel event is chosen to be the sum of green channel counts in the same time period obtained from the red channel event provided that no green channel event is identified within the same time period and vice versa. For coincidence events, we define a minimum time overlap for red and green channel events needs to be satisfied to be considered as a coincidence event. This minimum time overlap is chosen to be the residence time of Q_{dot} for a particular measurement because the spot size is at least one order magnitude larger than the size the protein complex. Unlike the non-coincidence events, the red and green channel values for coincidence events are the photon counts of their respect red and green events. Coincidence events and non-coincidence red, green channel events are then plotted together on the graph using different symbols. In this way, unbind and bind protein and protein complex events can be easily visualized and identified based on their spatial locations on the graph. The numbers of these different types of events can help quantify and dissect the dynamics of some important protein-protein interactions, which is very challenging with conventional techniques.

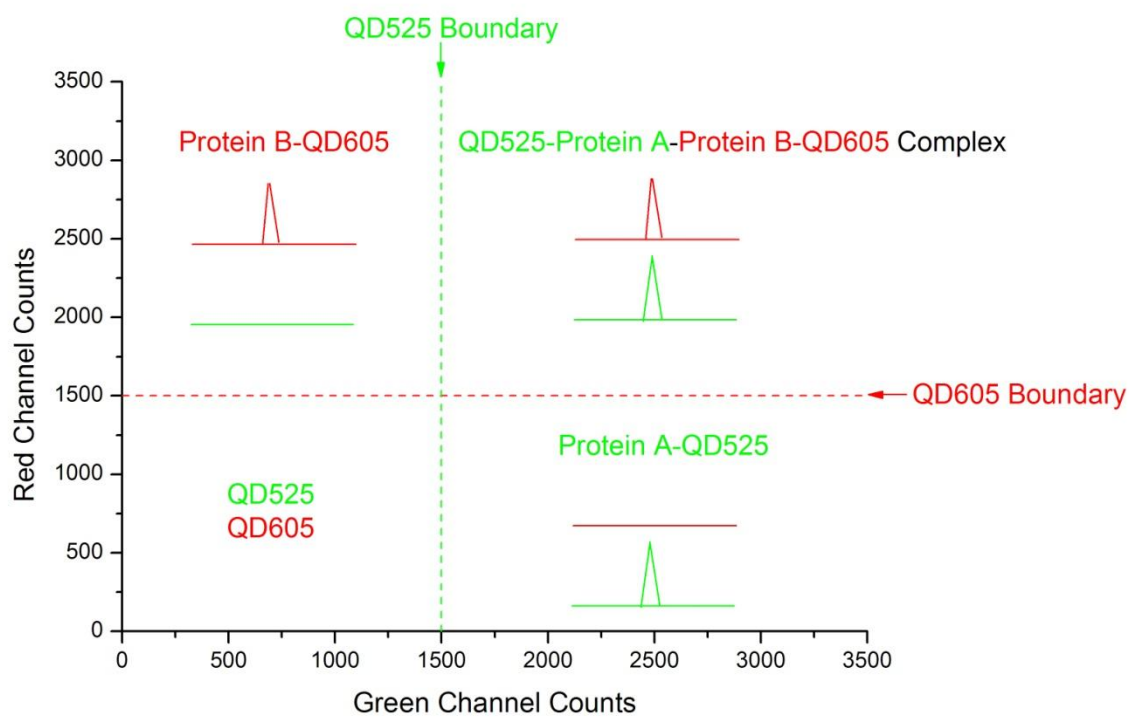


Figure 23 Principle of dual-color photon burst coincidence analysis to characterize the dynamics of protein-protein interaction.

6. MICROFLUIDIC TARGET PROTEIN DETECTION

6.1 Principle of detection

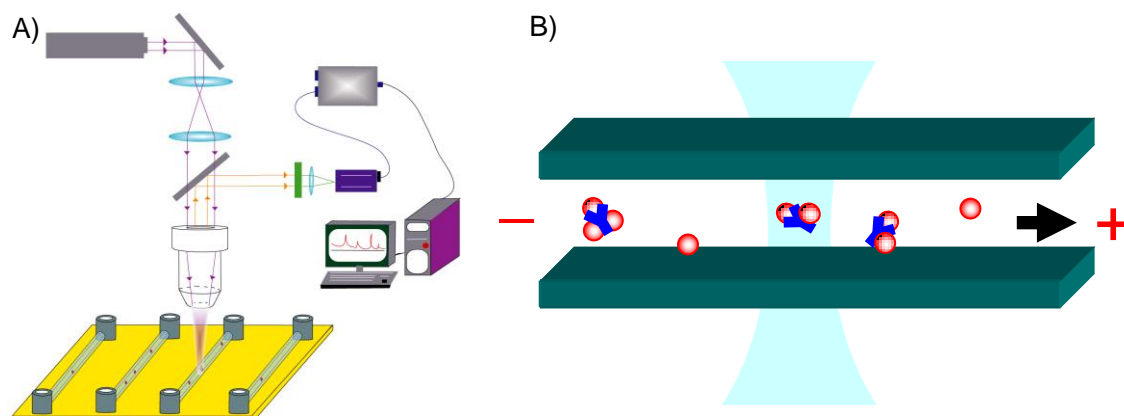


Figure 24 One-color single molecule flow proteometry. A) Schematics of system set-up; B) Qdots-protein complex flowing pass the detection volume under external electric field.

Figure 24 illustrates the schematics and detection principle of microfluidic one-color single molecule flow proteometry. Microfluidic channel with width of $2\mu\text{m}$ and depth of 500nm is used for all the experiments discussed in this section. Based on the autocorrelation fitting from bulk Qdot solution (no flow), an estimate laser spot size of $1\mu\text{m}$ is obtained. Assuming the detection volume is cylindrical in shape, 0.4 femto-liter is estimated for the detection volume. For a concentration of 1nM Qdots and assuming solution is homogenous, on average there is about 0.2 molecule in the focal volume, which ensures the single molecule resolution for our experiments. For all the target

protein detection experiments discussed in this study, a concentration of 1 nM or lower is used for Qdots.

The basic target protein detection principle is the use of polyclonal primary antibody to recognize target proteins. Polyclonal antibody is able to bind multiple epitopes that are available on the target protein. In this case, the target Hemagglutinin (HA) epitope tagged MAX cDNA was transfected and overexpressed in HEK293 cell line. Therefore, high concentration of MAX is expected in the cell lysate. These MAX proteins are tagged with multiple HA epitopes, which are specifically recognized by the primary anti-HA antibodies. As a result, more often than not, target HAMAX protein will be associated with more than one primary rabbit anti-HA antibodies.

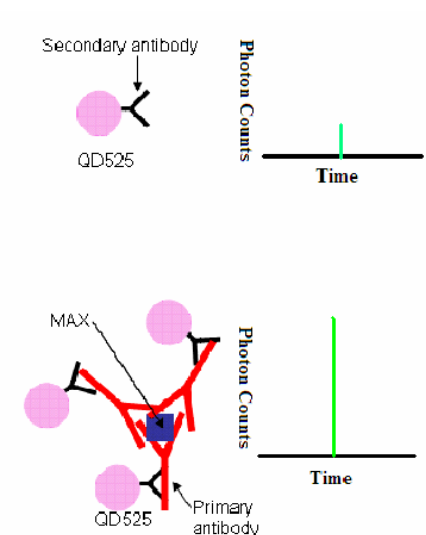


Figure 25 Target protein detection based on photon counts by using primary antibody of polyclonal nature.

Assuming each primary anti-HA antibody has at least one QD525 attached, target HAMAX protein will yield much higher fluorescence photon counts due to multiple QD525s comparing to single QD525, as shown in figure 25. For data analysis, the 2D photon burst plot of target protein sample is compared with that of the control sample. A characteristic 2D photon burst boundary is determined for control sample (Qdots with vector cell lysate) and events from target protein sample that are located outside the boundary are then identified as target proteins based on their photon counts. Number of these target protein events and their relative concentration can also be obtained and quantified in this way.

6.2 Qdots in microfluidic channel

Before target protein detection, QD525 are used to characterize the microfluidic channel, experiment conditions and data analysis procedures. 1nM QD525 in IP binding buffer solution is introduced to the microfluidic channel with a width of 2 μ m and depth of 500nm and external voltages ranging from 50V to 500V are applied to drive the solution. Figure 26 shows the autocorrelation of QD525 under various external fields and it suggests an increase in EOF flow as the voltage increases. Flow velocities are obtained by fitting these autocorrelation data to a 2D flow model built-in with the commercial FCS software. Flow velocities of $324.41 \pm 10.78 \mu\text{m/s}$, $680.38 \pm 23.92 \mu\text{m/s}$, $1362.24 \pm 49.24 \mu\text{m/s}$, $2054.81 \pm 71.61 \mu\text{m/s}$ and $155.64 \pm 106.05 \mu\text{m/s}$ are found for 50V, 100V, 200V, 300V and 500V, respectively.

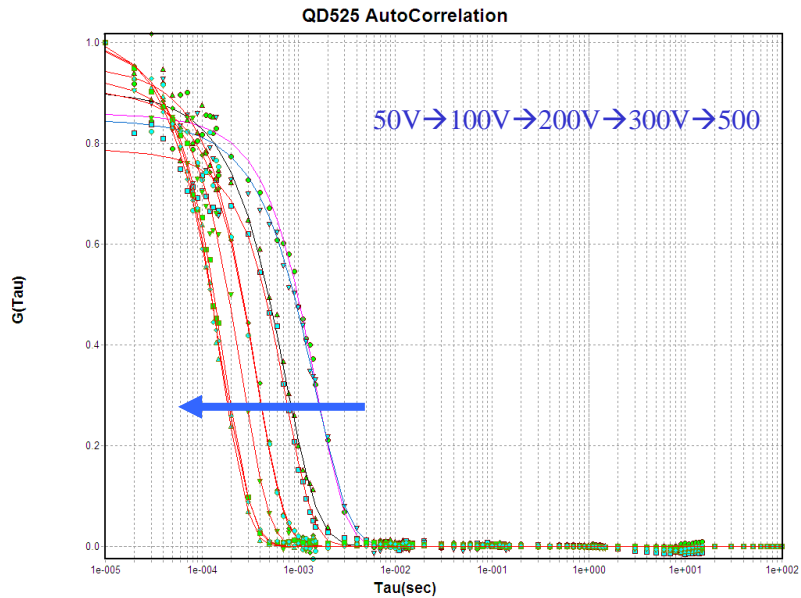


Figure 26 Autocorrelation of 1nM QD525 in microfluidic channel under external field ranging from 50V to 500V.

An empirical equation describing EOF velocity is as following [95],

$$V_{\text{EOF}} = \frac{\epsilon \zeta V}{d 4 \pi \eta} \quad (3)$$

where ϵ =dielectric constant of buffer, ζ =zeta potential, η =viscosity of buffer, V =voltage, d =channel length. As the equation suggests, EOF flow velocity is proportional to the applied voltage. Therefore, we plot the flow velocities obtained from the autocorrelation fitting as a function of applied voltages to verify the linearity, as shown in figure 27. An excellent linear relationship between the flow velocity and voltage is found in figure 27. This also suggests channel is in good working condition after PEI surface coating.

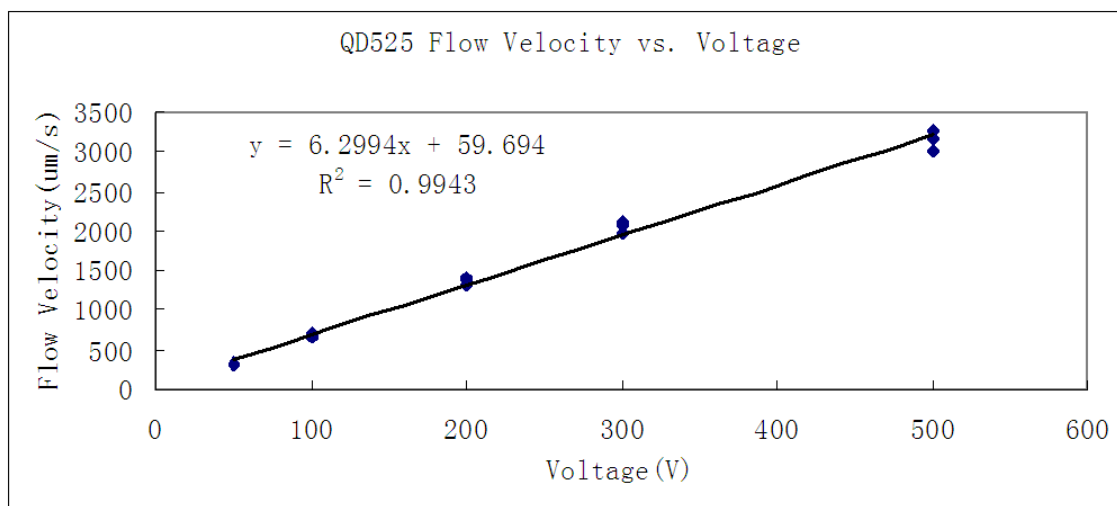


Figure 27 Linear fit of QD525 flow velocity as a function of voltages at 50V, 100V, 200V, 300V and 500V.

Furthermore, we analyze QD525 with three different concentrations in the microfluidic channel under 200V. The purpose is to verify our experiment procedures and data analysis methods in terms of concentration analysis. 469 ± 13 , 1743 ± 51 and 4933 ± 93 QD525 events are identified for QD525 concentrations of 0.5nM, 2nM and 5nM, respectively. This result shows excellent linear relationship as well as the same proportion between number of events identified and QD525 concentration, as shown in figure 28. The standard deviation is very small for all measurement as well, which suggests a steady homogenous flow and not much variability associated with different microfluidic channels. Same data were also analyzed without performing the moving average operation. The results (not shown here) in terms of number of identified QD525 events doesn't vary linearly with the concentration values. Therefore, the moving average operation is very critical for our concentration analysis and numbers of single

molecule events identified reflect the relative concentration of target molecules in the solution.

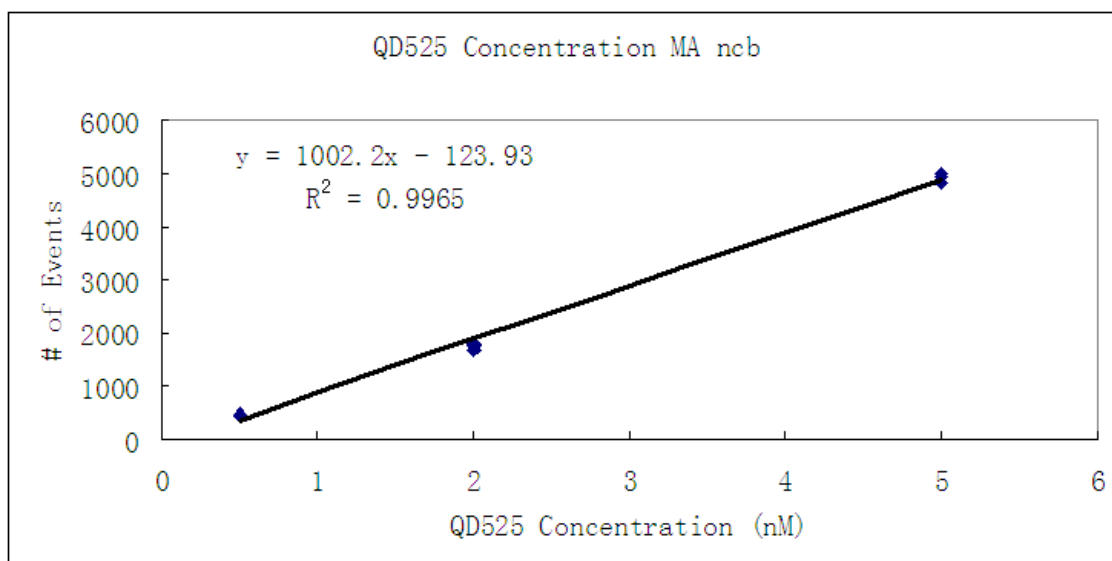


Figure 28 Linear fit of number of QD525 events identified (moving averaged) as a function of QD525 concentration.

6.3 Detection of HAMAX and its concentration analysis

In this section, we demonstrate the detection of target protein HAMAX and characterization of HAMAX concentration direct from cell lysate based on our 2D photon burst analysis. $2\mu\text{m}$ -wide microchannel is used for this experiment and the cell lysate contains over-expressed HAMAX proteins.

Figure 29 shows the flow velocities as a function of applied voltages for the HAMAX samples and good linear relationship is found between these two variables, which suggests a stable surface coating during detection.

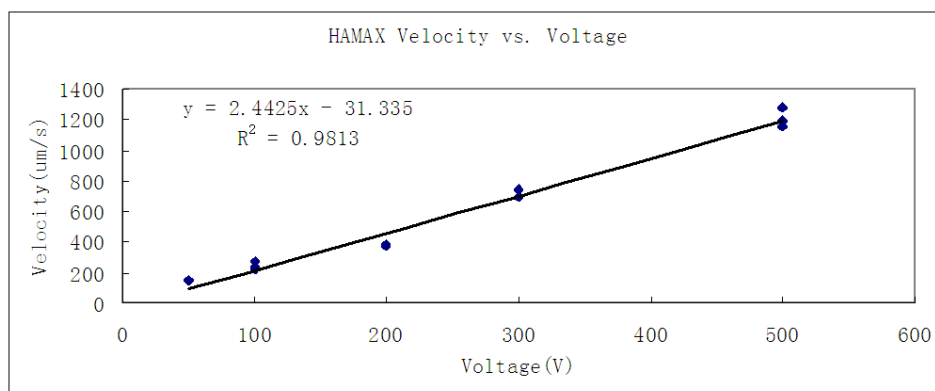


Figure 29 Linear fit of QD525-HAMAX flow velocity as a function of voltages at 50V, 100V, 200V, 300V and 500V.

Photon bursts of HAMAX sample under 200V and 500V are also shown in figure 30. As expected, photon bursts at 500V are more frequent and have less photon counts per burst comparing to photon bursts at 200V due to higher flow velocity. Since flow and signals are relatively stable at 200V based on our observation, most of the data presented here with 2 μ m-wide microchannel is under an external voltage of 200V. To identify HAMAX target protein from cell lysate, three samples are prepared, QD525 in IP binding buffer, QD525 with vector cell lysate (no HAMAX present) in IP binding buffer and QD525 with HAMAX over-expressed cell lysate (high concentration of HAMAX present) in IP binding buffer. Samples are introduced to three identical microfluidic channel and their photon burst signals are recorded under 200V.

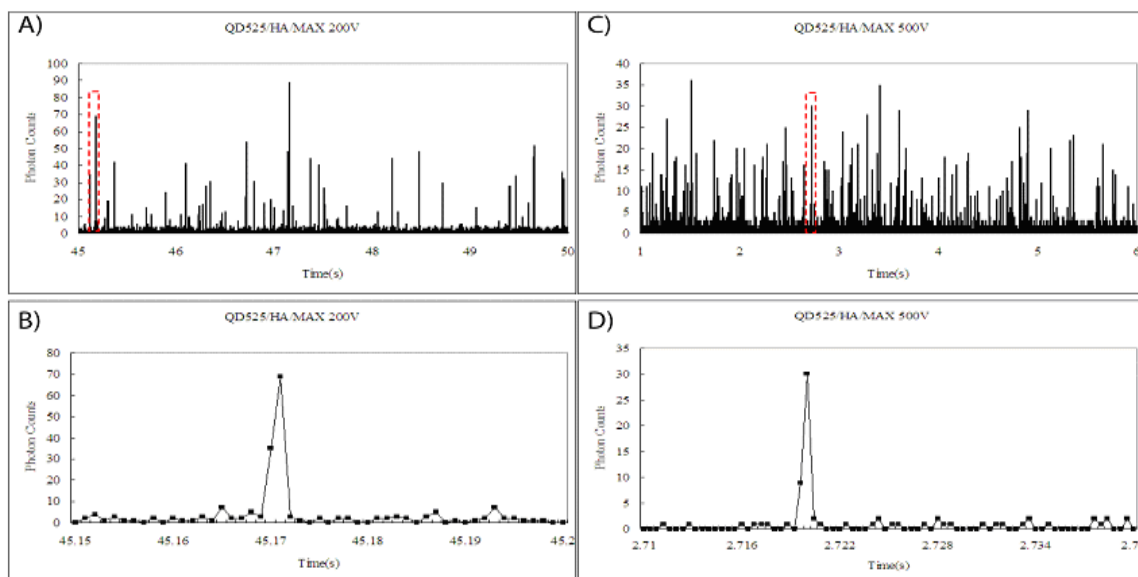


Figure 30 HAMAX photon burst as a function of time at 200V (A) and 500V (B), magnified peaks at 200V(C) and 500V (D).

Raw data for each sample is analyzed by 2D photon burst analysis described in the previous section and results are shown in figure 31. Legend QD525, VCELL and HAMAX refer to pure QD525, QD525 with vector cell lysate and QD525 with HAMAX over-expressed cell lysate. From this 2D plot, HAMAX sample contains much more events with significantly high photon counts comparing to the pure QD525 sample, which is explained by multiple QD525 association with HAMAX due to the polyclonal nature of the primary anti-HA antibody. To verify these high-photon-count events are in fact from HAMAX, 2D photon burst diagram of QD525 with vector cell sample, which is the same cell lysate containing almost no HAMAX protein but only the primary anti-HA antibodies, is also plotted. VCELL shows similar events distribution on the 2D plot

with the pure QD525 sample (figure 31), which suggests no significant non-specific binding of the primary antibody is found in the cell lysate.

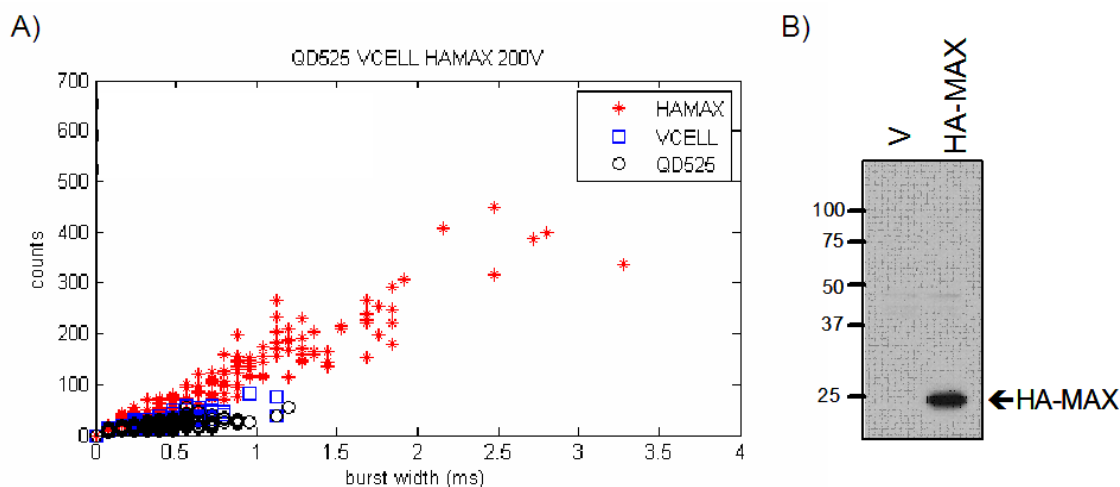


Figure 31 Detection of HAMAX target protein. A) 2D photon burst plot consisting of pure QD525, vector and HAMAX sample at 200V. B) Conventional western blot confirming the absence and existence of HAMAX in vector and HAMAX samples, respectively.

Conventional western blot results shown in figure 31B confirm the absence of HAMAX in vector sample and the existence of HAMAX in HAMAX sample (black band on the right lane). Therefore, we can conclude that those high-photon-count events in HAMAX sample are indeed from multiple QD525s attached HAMAX proteins and the apparent difference in events distribution on the 2D photon burst diagram suggests the existence and successful detection of HAMAX protein in cell lysate. Figure 32 shows typical photon burst peaks from pure QD525, vector and HAMAX cell samples. Photon burst peaks of pure QD525 and vector sample share similar magnitude while

photon burst peak of HAMAX is significantly higher, which is consistent with the conclusion obtained from the 2D photon burst analysis.

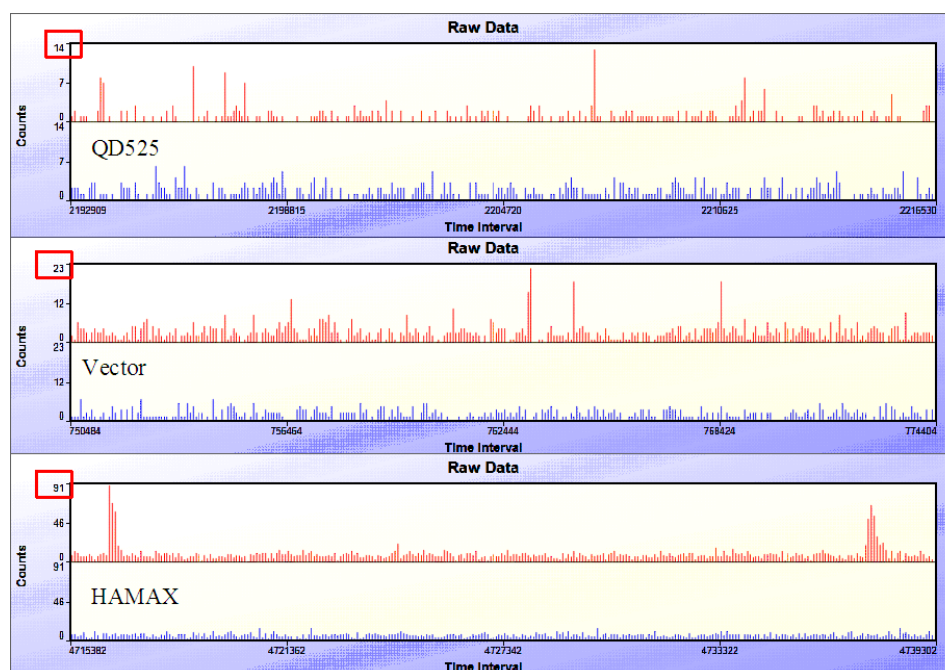


Figure 32 Photon burst peaks of pure QD525, vector and HAMAX sample at 200V with an integration time of 1 millisecond.

Qualitatively, we are able to detect the presence of HAMAX direct from cell lysate based on the spatial distribution of single molecule events on the 2D photon burst plot. Furthermore, this 2D photon burst analysis allows us quantitatively analyze the concentration of target protein, such as HAMAX, based on the number of identified events as well. To identify target protein events, a characteristic QD525 boundary in terms of photon counts and burst width can be defined. Assuming the distribution of photon counts and burst width of QD525 events are normal, we set the boundary as three

standard deviations from the mean values, as shown in figure 33. From a statistics point of view, the chance of a QD525 event on the 2D plot lies outside this boundary is smaller than 0.2%. In this way, after applying the QD525 boundary to HAMAX sample and counting the events that are outside the boundary, we can obtain the number of HAMAX events for a particular measurement, thus the relative concentration.

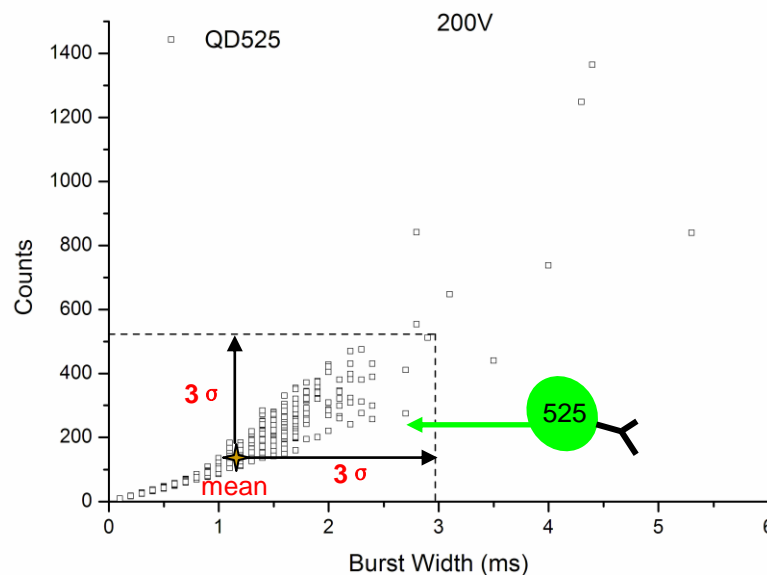


Figure 33 Determination of photon burst and burst width of QD525 boundary at 200V.

To verify this approach, we prepared three HAMAX samples, including cell lysate with 1 μ g, 5 μ g and 10 μ g transfection DNA. More HAMAX transfection DNA will result in cell expressing more HAMAX protein, thus a higher concentration of HAMAX in cell lysate. 2D photon burst analysis is performed for all three samples and numbers of events outside the QD525 boundary are obtained. Figure 34 shows the 2D photon

burst plots of HAMAX events from all three samples and an increase of HAMAX events are found as the amount of transfection DNA increases.

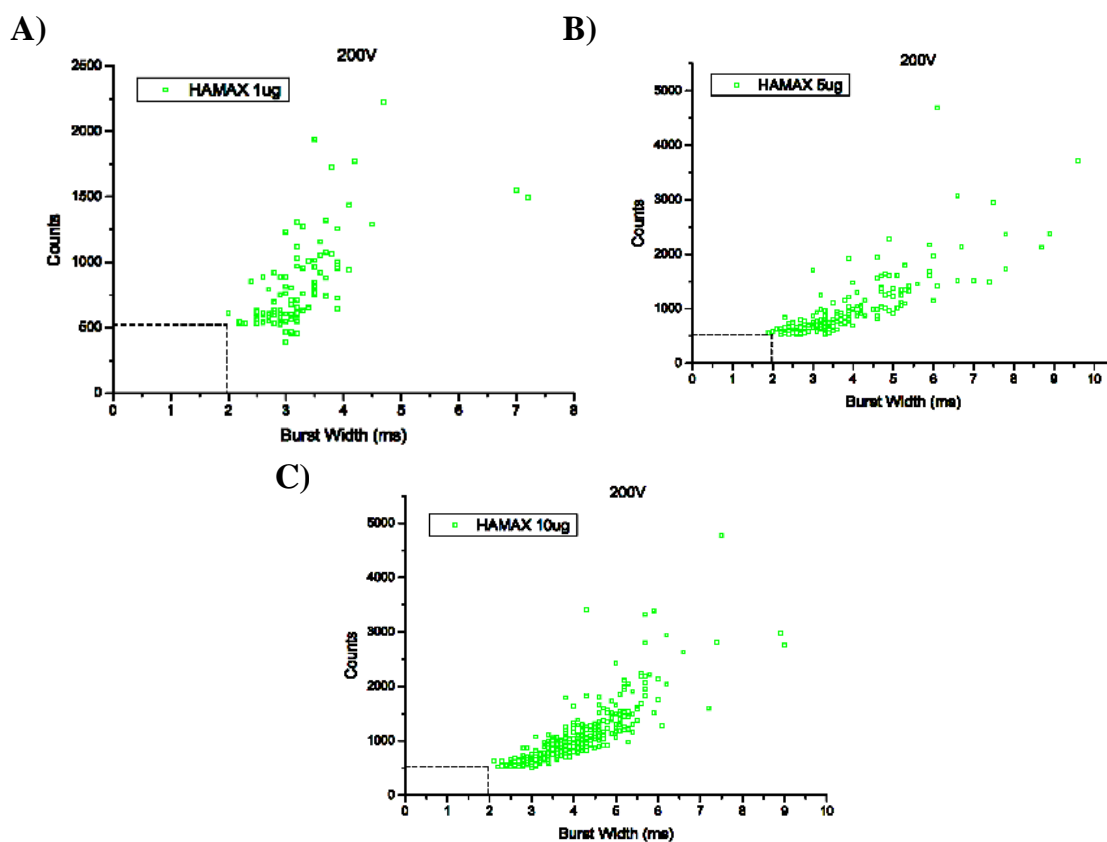


Figure 34 2D photon burst plots of HAMAX events from cell lysate of 1µg (A), 5µg (B) and 10µg (C) transfection DNA. QD525 boundary in figure 33 plotted as dotted black rectangles and an increase number of HAMAX events are detected.

Averages of 34.7 ± 6.5 , 72.3 ± 9.1 and 129.3 ± 5.9 HAMAX events for each measurement are identified for cell lysate with 1µg, 5µg and 10µg transfection DNA, respectively. As expected, increase in transfection DNA amount leads to increase in the number of events identified from the 2D photon burst analysis as HAMAX

concentration in cell lysate increases. Since the flow velocities for these three samples are somewhat different, we need to normalize the average number of HAMAX events for each sample by its flow velocity and normalized averages of 34.7 ± 6.5 , 123 ± 15.5 and 224.5 ± 10.2 HAMAX events are obtained for cell lysate with $1 \mu\text{g}$, $5 \mu\text{g}$ and $10 \mu\text{g}$ transfection DNA, respectively. Figure 35 shows an excellent linear relationship between the normalized average number of HAMAX events and amount of transfection DNA. Other fluorescence spectroscopy parameters such as $G(0)$ and CPS obtained from the same measurements were used to characterize the HAMAX concentration and compare with our photon burst analysis technique. $G(0)$ is parameter from autocorrelation and inversely proportional to the number of molecule in the detection volume. CPS is the average counts per second value for a particular measurement. However, the linear model goodness of fit $G(0)$ ($R^2=0.7027$) and CPS ($R^2=0.8217$) as function of HAMAX concentration are not nearly as good as our photon burst analysis technique ($R^2=0.9994$).

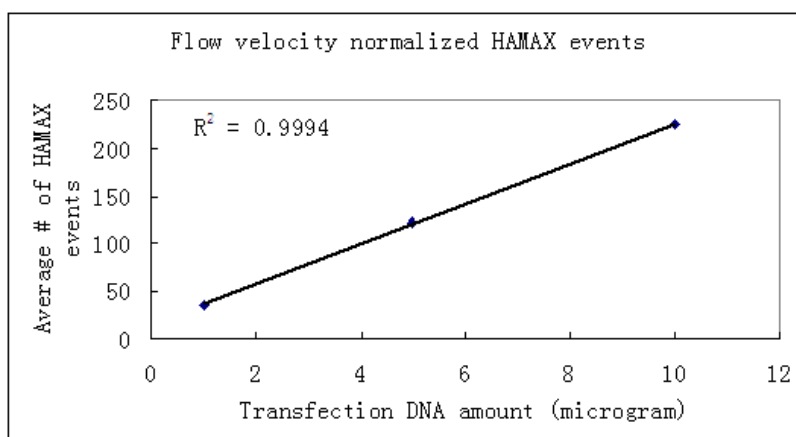


Figure 35 HAMAX concentration analysis and normalized average number of HAMAX events as a function of transfection DNA amount.

Therefore, our single molecule photon burst analysis method yields a better and more accurate measurement on target molecule concentration. In addition, we carried out a similar concentration analysis, where HAMAX concentration is simply varied by controlling the concentration of cell lysate in IP buffer. It also confirms that more HAMAX events are identified in sample with higher cell lysate concentration and detailed results can be found in Appendix B.

In a word, we had developed a microfluidic single molecule technique to detect target proteins, in particular HA epitope tagged MAX protein, direct from cell lysate without any prior purification process based on the polyclonal nature of the primary antibodies used to recognize the target protein and 2D photon burst analysis. The entire processing time of this detection approach is about 2-3 minutes, which is significantly shorter comparing 2-3 days of conventional techniques, i.e. IP and western blot. More importantly, with this technique we are counting individual molecule events and are thus able to quantify and characterize the concentration of the target protein with high resolution.

7. NANOFUIDIC PROTEIN INTERACTION STUDY

7.1 Principle of detection

In this section, we focus on the detection and characterization of protein interaction. A one-color scheme based on 2D photon burst analysis is introduced to study interaction between two proteins and a dual-color photon burst coincidence analysis technique is also presented for both two-protein and three-protein interaction detections.

7.1.1 One color scheme

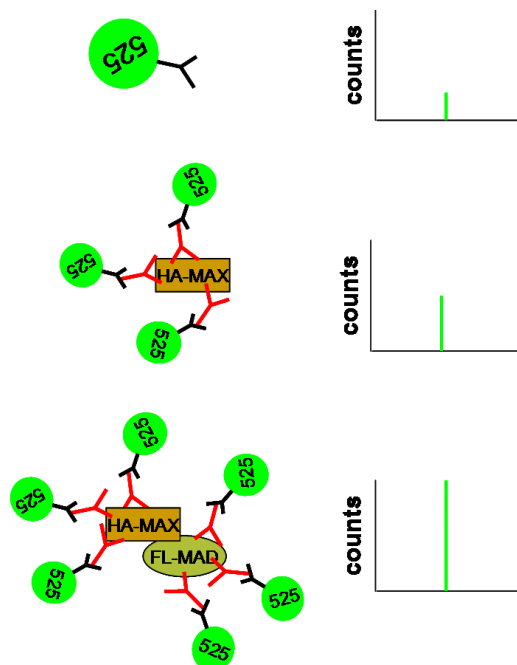


Figure 36 One-color protein interaction detection based on photon counts by using primary antibody of polyclonal nature.

Here we describe a one color scheme based on the 2D photon burst analysis to study protein interaction and its principle of detection is shown in figure 36. Same as the target protein detection presented in the previous section, we use polyclonal primary antibody to recognize target proteins. In this case, two primary polyclonal antibodies are used to recognize each interacting protein and both primary antibodies are associated with QD525. As a result, if the two proteins interact and form a complex, the signal from the complex should have a higher photon counts comparing to the signal of individual protein with QD525 or single QD525 events. Again, 2D photon burst analysis is used to compare photon counts and burst width of single molecule events from different samples to detect potential interactions.

7.1.2 Dual color scheme

One of the most common spectroscopy techniques to detect protein interaction is to label two interacting proteins with dyes of two different colors. Fluorescence crosscorrelation spectroscopy or coincidence analysis is used to assess the interaction based on the time scale similarity of signals from both channels. In other words, if the two proteins interact and form a complex, as it passes through the focal volume, both dyes should emit fluorescence and signals should register in both channels at the same time. By analyzing these coincidence events, one can assess the interaction between these two proteins. Figure 37 shows the schematics of the dual-color detection system used in this study. However, without additional data analysis techniques, it's hard to quantify the interaction dynamics, for example, the binding ratio between interacting proteins. In the earlier section, we introduced the dual-color photon burst coincidence

analysis technique, which plots both coincidence and non-coincidence single molecule events in terms of their photon counts from both channels. This technique combines coincidence analysis with polyclonal target protein detection scheme we had developed and allows us to identify the number of target protein in either free form or complex form interacting with the other target protein, therefore assess the interaction dynamics. Furthermore, combining the one-color protein interaction detection scheme described earlier with the dual-color photon burst coincidence analysis, we are able to detect and assess interaction between three proteins or even four proteins with only two color labels.

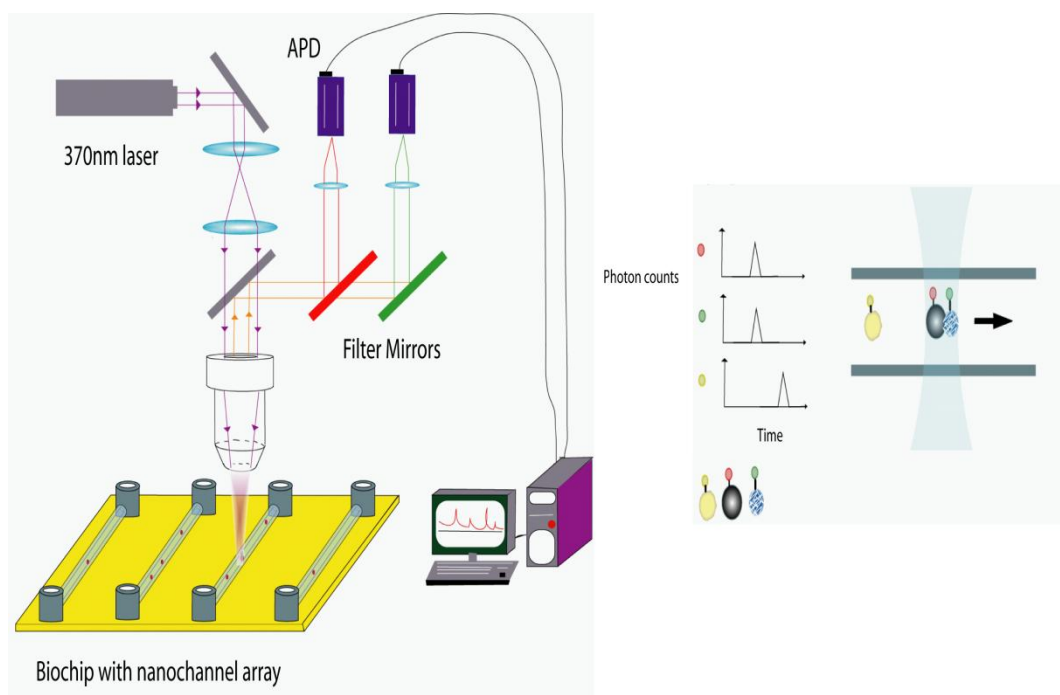


Figure 37 A dual-color fluorescence single molecule detection system for multiple protein interaction study and its coincidence analysis.

7.2 Model protein

Since we are developing a novel technique to study protein interaction, proof-of-principle experiments with model proteins that have well-known binding interaction are necessary to validate our approach. Here we present the characterization of two well known interactions between protein MAX and protein MAD, protein MYC and protein MAX from the lysate of HEK293 cell with our techniques.

7.2.1 MAX-MAD interaction study by one color scheme

HA epitope tagged MAX (HAMAX) and Flag (FL) epitope tagged MAD (FLMAD) are co-transfected and overexpressed in HEK293 cell. These two proteins are well known for interaction and forming complex in cell. To verify this, we carried out a dual color experiment to detect the complex existence. First, before tagging protein with primary antibody and Qdots, we tested the affinity between Qdot secondary anti-rabbit antibody and primary rabbit antibody. Figure 38A shows the photon burst peaks of individual QD605 and QD525 events as well as coincidence events from anti-rabbit QD525/QD605 complex interacting through rabbit primary antibody. Next, we label HAMAX with the secondary anti-rabbit QD525 through the primary rabbit anti-HA antibody and FLMAD with the secondary anti-mouse QD605 through the primary mouse anti-FL antibody. Since anti-rabbit antibody only recognizes rabbit antibody of the same species, QD525 will only bind to HAMAX while QD605 will only bind to FLMAD, as shown in the cartoon of Figure 38B. We were also able to detect the QD525 and QD605 coincidence events, which verify the binding between MAX-MAD.

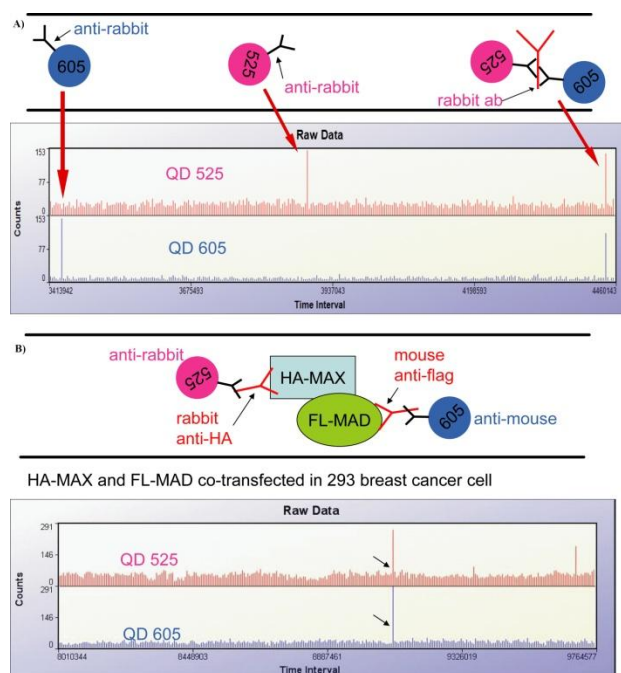


Figure 38 QD525 and QD605 photon burst coincidence. A) QD525 and QD605 interaction through primary antibody of the same species; B) HAMAX and FLMAD interaction indicated by coincidence of QD525 and QD605.

For one-color MAX-MAD detection, as described earlier, we rely on discrimination based on the photon counts of MAXMAD events. Unlike the two color scheme above, the primary anti-HA and anti-FL antibodies used to recognize HAMAX and FLMAD, respectively, are both from rabbit and polyclonal in nature. As a result, secondary anti-rabbit QD525s are able to bind to both HAMAX and FLMAD through the primary antibodies. A higher photon counts are expected for MAX-MAD events due to more QD525s are associated. To identify MAX-MAD complex, individual baseline samples, such as pure QD525, HAMAX/QD525 and FLMAD/QD525, need to be characterized. Figure 39A shows the 2D photon burst plot of QD525 and its characteristic boundary. With this QD525 boundary, we identify HAMAX and FLMAD

events with the same technique discussed in section 6. Assuming distribution of HAMAX and FLMAD events on 2D photon burst diagram is also normal, we apply the same statistical analysis for pure QD525 on HAMAX and FLMAD to obtain their characteristic boundaries, as shown in figure 39B. For MAXMAD sample, we first apply the QD525 boundary and events that lie outside of the boundary are considered as HAMAX, FLMAD or MAXMAD events.

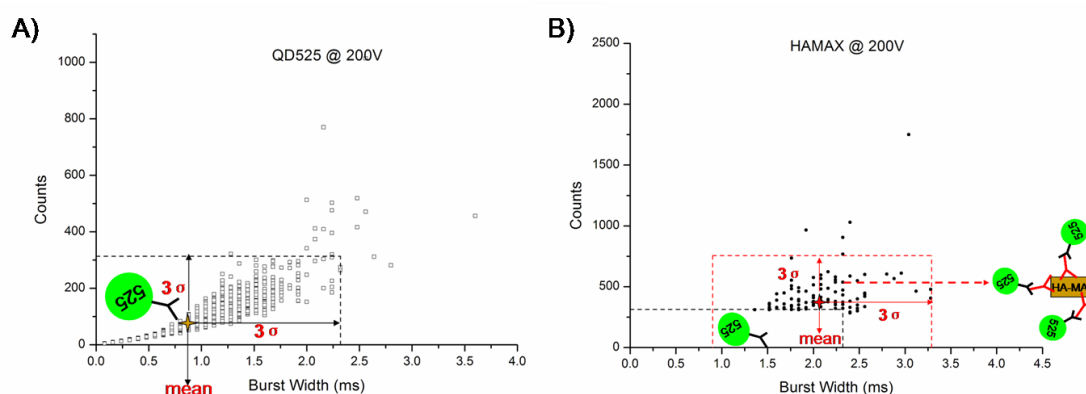


Figure 39 2D photon burst diagram of QD525 (A) and HAMAX (B) at 200V. Pure QD525 boundary (black dotted rectangle shown in A) and HAMAX boundary (red dotted rectangle shown in B).

Next, we apply the HAMAX and FLMAD boundaries on these protein and protein complex events and events that lie outside out of both boundaries are then considered as MAXMAD interaction events. Figure 40 demonstrates the successful detection of HAMAX-FLMAD complex based on 2D photon burst analysis. From a total of three measurements of MAXMAD sample, with the previous vector QD525 boundary we obtained the number of total protein events including, HAMAX, FLMAD proteins

and MAXMAD complex proteins and with HAMAX and FLMAD boundaries, we obtained the number of MAXMAD complex events. Considering the systematical error in determining boundary conditions, a range from 7-10% of the total MAX and MAD proteins are forming MAXMAD complex.

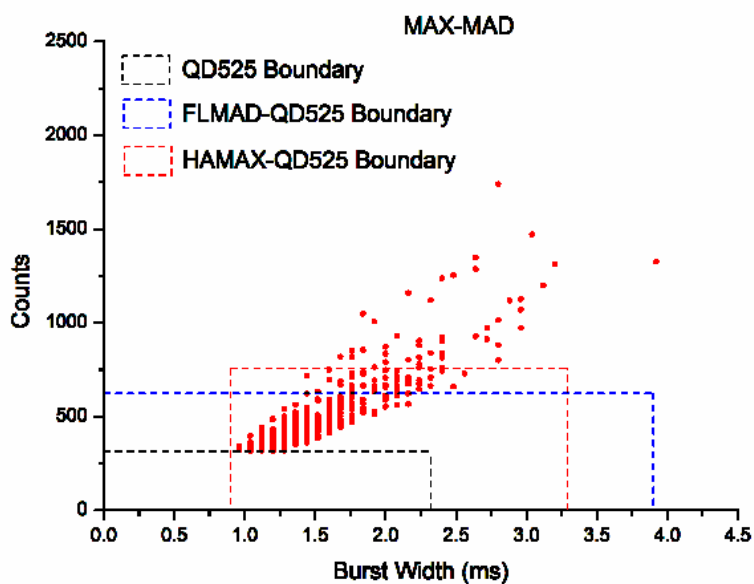


Figure 40 2D photon burst diagram of HAMAX-FLMAD and one-color detection of MAX-MAD interaction.

In summary, we have successfully demonstrated the detection of two-protein interaction by using only one fluorescence label and 2D photon burst analysis based on the photon counts of single molecule events. Their interaction dynamics in terms of binding ratio is also obtained.

7.2.2 MYC-MAX interaction study by one color and dual color schemes

MYC and MAX proteins are also known to form complex inside the breast cancer cell. In this section, we present the study of MYC-MAX interaction by both one color and dual color schemes. MYC and HA epitope tagged MAX are co-transfected and overexpressed in HEK293 cell. Polyclonal primary rabbit anti-HA and anti-MYC antibodies are added in the cell lysate to bind to MYC and HAMAX proteins. Secondary anti-rabbit QD605s recognizing both rabbit anti-HA and anti-MYC primary antibodies are then added in the cell lysate as fluorescence label. The one-color detection scheme and data analysis method are identical as for those used in MAX-MAD interaction study. 2D photon burst analysis results are shown in figure 41. A total number of 938 protein events are found for individual MYC, HAMAX or MYC-MAX complex for a total of three measurements. Among all the MYC and MAX proteins in HEK293 cell, 7%-8.1% are forming MAX-MYC MYC-MAX complex.

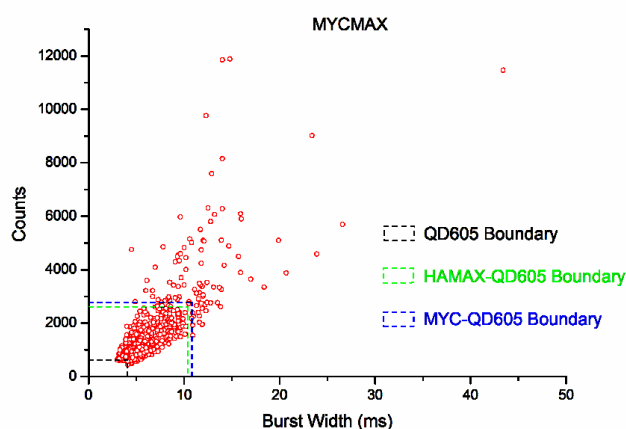


Figure 41 2D photon burst diagram of HAMAX-MYC and one-color detection of MAX-MYC interaction.

Since the interaction dynamics of MAX-MYC has not been reported, to verify this one-color detection scheme, we label HAMAX with QD525 and MYC with QD605 and use dual-color photon burst coincidence analysis to perform the same MYC-MAX interaction study. We have described the dual-color photon burst coincidence analysis in previous sections and figure 42 shows the detection principle in particular for MYC-MAX interaction. Based on the spatial locations of single molecule events on the dual-color coincidence plot, one can determine the number of each type event, including MYC, HAMAX and MYC-MAX, thus assess the interaction dynamics.

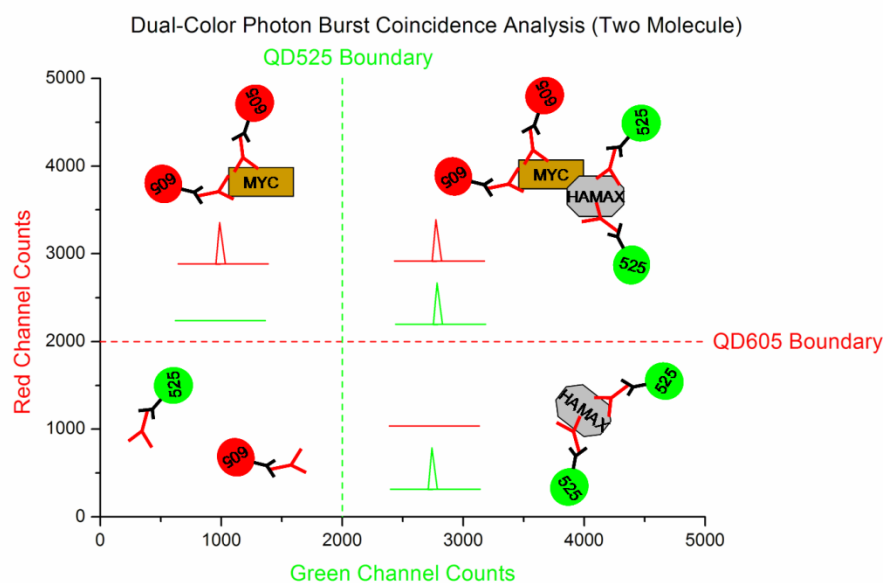


Figure 42 Detection principle of two-protein interaction (MYC-MAX) with dual-color photon burst coincidence analysis.

To do this, the very first step is to determine the boundary counts for QD525 and QD605, the dotted red and green lines as shown in figure 42. Vector cell lysate sample

containing no target proteins and only QD525/QD605 are analyzed. Three standard deviations from the mean counts for both red and green channel are used as boundary counts, as shown in figure 43. Although there are some events which lie outside the QD525 and QD605 boundary, the percentage is less than 1% for this case and it could be due to some non-specific binding in cell lysate.

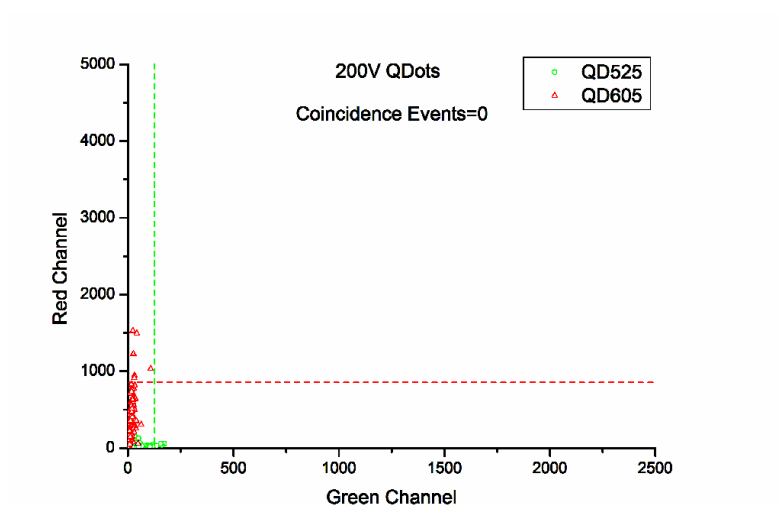


Figure 43 Dual-color photon burst coincidence plot of vector cell lysate sample containing only QD525 and QD605. QD525 and QD605 boundary counts are drawn on the plot as dotted green and red lines, respectively.

Once the Qdot counts boundaries are set, cell lysate containing QD605/primary antibody anti-MYC recognizing MYC and cell lysate containing QD525/primary antibody anti-HA recognizing HAMAX are analyzed separately. The dual-color photon burst analysis of these two samples is shown in figure 44. As expected, almost no coincidence events are detected for both samples.

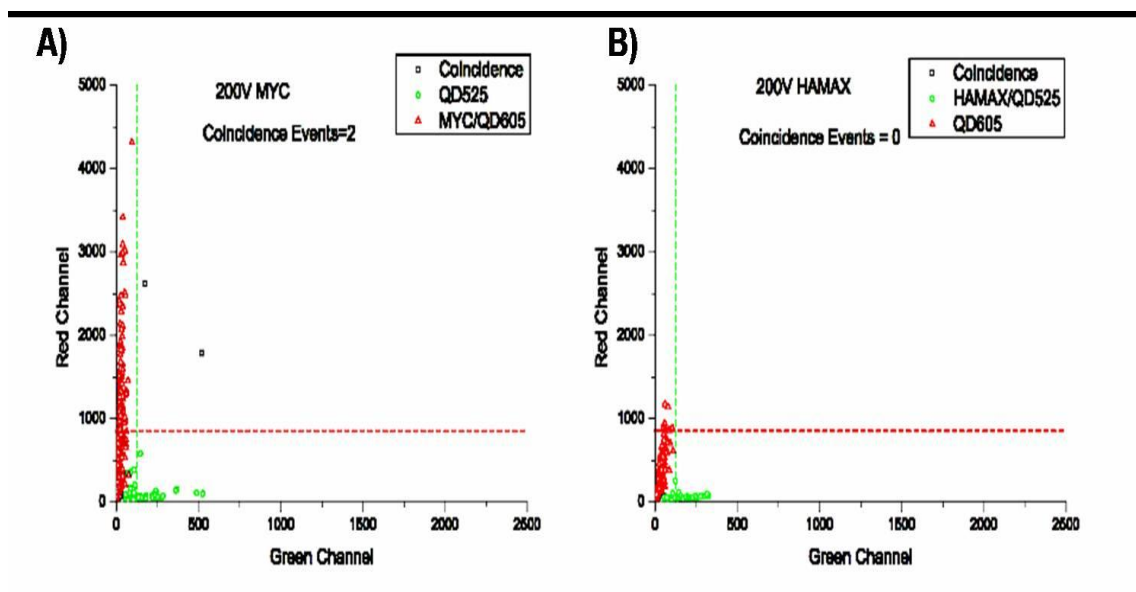


Figure 44 Dual-color photon burst coincidence plots of MYC (A) and HAMAX (B) samples.

Finally, we add both primary antibody anti-MYC and anti-HA in the cell lysate along with QD525 and QD605. The dual-color photon burst coincidence analysis of MYC-MAX is shown in figure 45. Among all the MYC and MAX proteins detected in HEK293 cell, 25.1%-26.1% are free MAX proteins, 60.3%-65.7% are free MYC proteins and 6.8%-8.2% are forming MYC-MAX complex, which is in excellent agreement with the result (7%-8.1%) obtained from one-color detection scheme on the same MYC-MAX sample.

In summary, we have demonstrated the detection of MYC-MAX two-protein interaction by both one-color photon burst analysis scheme and dual-color photon burst coincidence analysis scheme. In addition, the interaction dynamics in terms of binding ratio obtained with these two different techniques are in very good agreement.

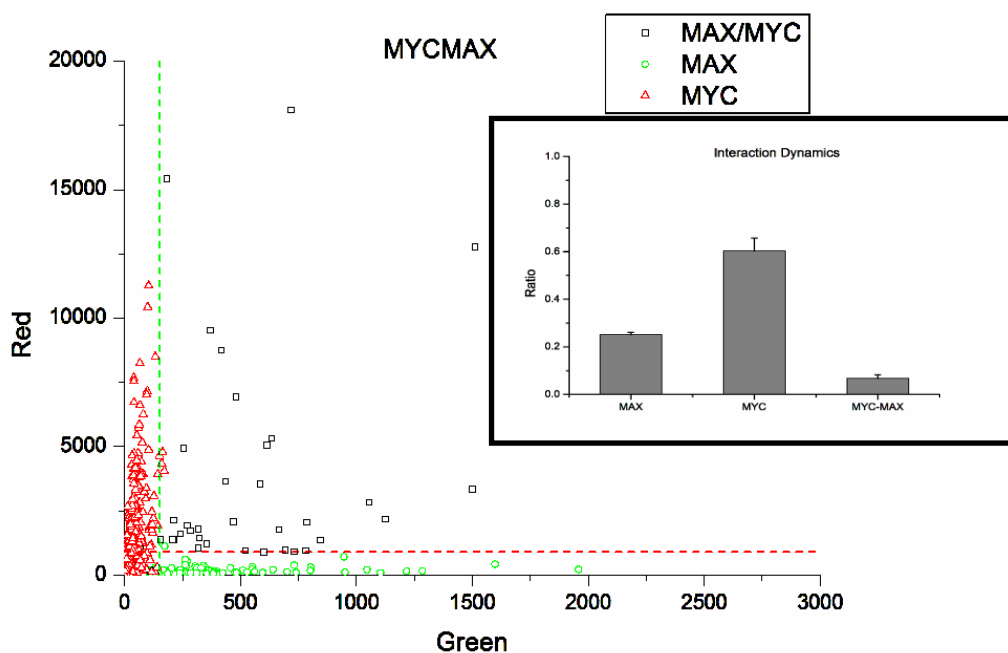


Figure 45 Dual-color photon burst coincidence analysis of MYC-MAX sample. Inset: interaction dynamics represented in bar graph.

7.3 Cancer related protein

Studies of model proteins with well-known interaction characteristics are necessary to validate our detection approach, but it lacks of clinical importance in terms of cancer research. In this section, we are attempting to apply this technique on cancer related proteins to study their interactions in hope to answer some of the questions that were very challenging for conventional techniques. EGFR is an important membrane protein responsible for triggering downstream tumor signal transduction by interacting with other proteins inside the cell. Therefore, it could be of great importance to study the interactions of EGFR protein to dissect the tumor signal pathways in breast cancer cell.

7.3.1 Detection of EGFR protein and concentration analysis

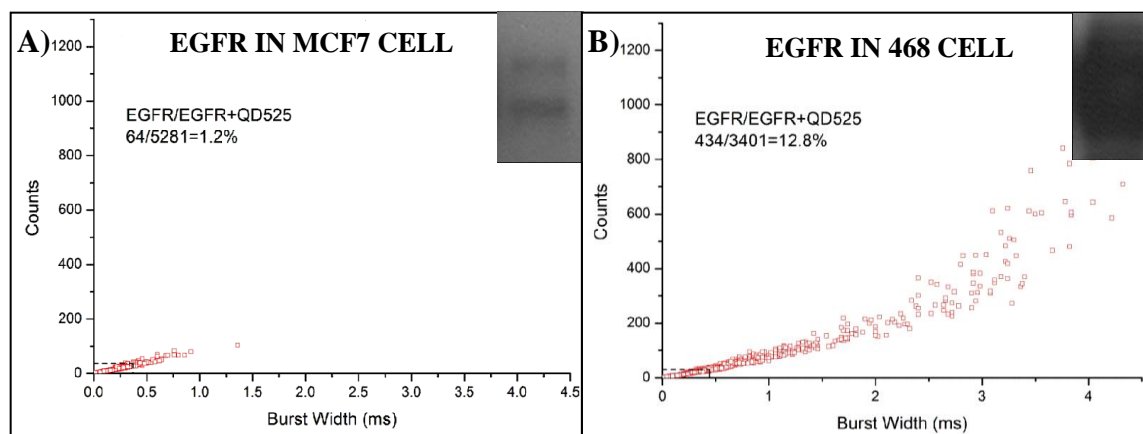


Figure 46 Detection of target EGFR protein in different cells. A) 2D photon burst diagram of EGFR in MCF7 cell, inset: IP/western blot of EGFR in MCF7 cell; B) 2D photon burst diagram of EGFR in 468 cell, inset: western blot of EGFR in 468 cell.

There are several polyclonal primary antibodies available for targeting EGFR protein from conventional IP study and one of the polyclonal primary antibodies called ab13C is chosen for its better performance with our technique (data not shown). To demonstrate the detection of EGFR protein, we carried out experiments on lysates from two different cells, MCF7 and 468. Based on traditional western blot studies, MCF7 cell contains much less endogenous level EGFR than those of the 468 cell and their western blots are presented in figure 46C, as 468 cell showing significant EGFR band on the left lane. The 2D photon burst analyses of these two cells in terms of EGFR concentrations also confirm the results from IP study, as shown in figure 46 A and B. Under the same Qdot concentration, only 1.2% of all the events are identified as EGFR protein for MCF7 cell while 12.8% of all the events are identified as EGFR protein for 468 cell.

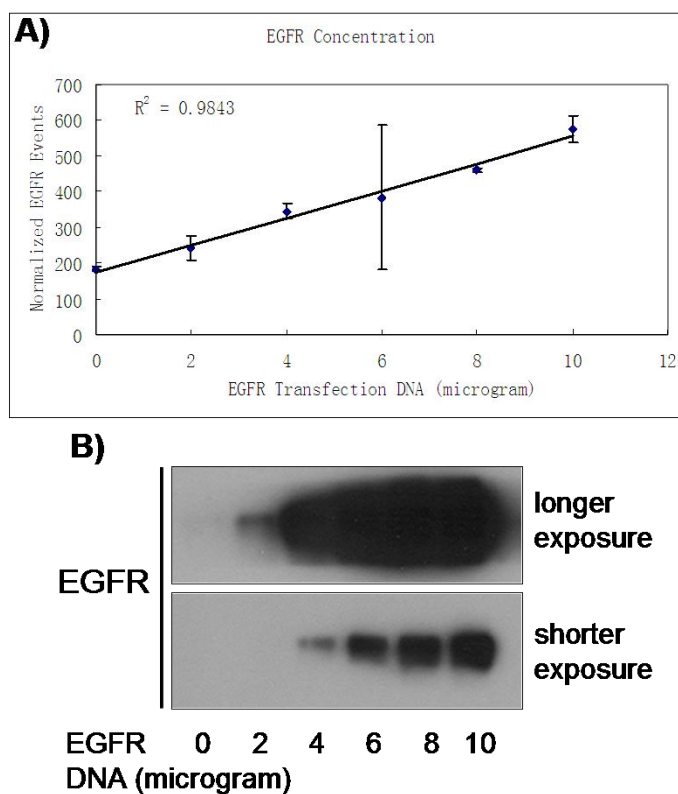


Figure 47 EGFR concentration analysis. A) normalized EGFR protein events as a function of transfection DNA amounts, error bar indicates the standard deviation. B) traditional western blot of EGFR proteins from the same samples.

Similar for HAMAX concentration study in the previous section, we overexpress EGFR protein in HEK293 cell with EGFR-expressing DNA. Cell lysates with 0 μ g (endogenous level), 2 μ g, 4 μ g, 6 μ g, 8 μ g and 10 μ g transfection DNA were analyzed with both our single molecule technique and traditional western blot method. Results are shown in figure 47 and same linear relationship between EGFR transfection DNA amount and normalized EGFR events are found, as shown in figure 47A. Results from traditional western blot method were shown in figure 47B. For a shorter exposure time,

concentrations of EGFR proteins from cell lysates with 0 μ g and 2 μ g EGFR DNA were too low to be detected with this technique. For a longer exposure time, 2 μ g could be seen. However, signals from 6 μ g, 8 μ g and 10 μ g become saturated due to overexposure. Comparing with the traditional method, our single molecule technique shows significantly higher sensitivity, which leads to improvement in detection limit and detection resolution for target protein. Figure 47A shows a very good fit for linear model, however, the data point of 6 μ g displays an abnormally high standard deviation. We are currently investigating this issue and more experiments are underway. The reason we suspect at this moment is due to QD605 aggregation causing flow instability.

7.3.2 Dual-color detection of SRC-EGFR-STAT3 three-protein interaction---a preliminary study

SRC and STAT3 are the two proteins that known to interact with EGFR inside the cancer cell. Current cancer research had revealed evidences showing the existence of EGFR/SRC and EGFR/STAT3 complex. Researcher had proposed the possibility of forming SRC/EGFR/STAT3 complex because SRC and STAT3 bind to EGFR at different binding sites. However, up until now, it's still unclear if there is formation of SRC/EGFR/STAT3 three-protein complex in cancer cell due to unavailability of current techniques to probe three-protein interaction. With this dual-color photon burst coincidence analysis technique, we hope to shed some new light and test the hypothesis of formation of SRC/EGFR/STAT3 three-protein complex in cancer cell. As for experimental details, we chose to use a smaller nanofluidic channel, which has a width

of 500nm at the detection region. The depth is still 500nm. As stated earlier, narrower channel will lead to better signal-to-noise ratio and more uniform excitation of Qdots. Due to channel length difference, instead of 200V, we apply 100V for the experiments with 500nm-wide channels.

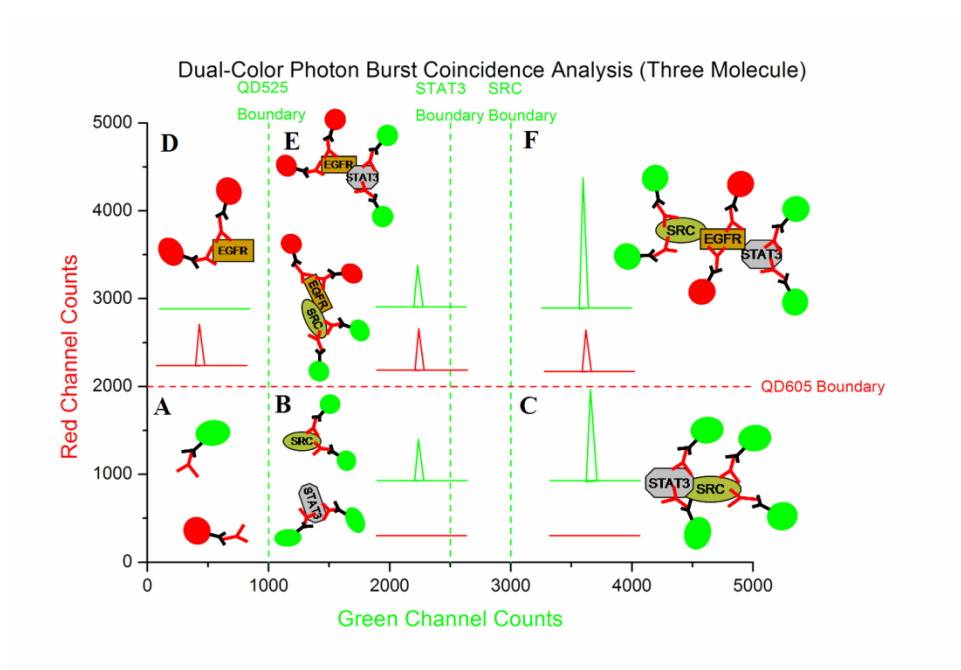


Figure 48 Detection principle of three-protein interaction (SRC-EGFR-STAT3) with dual-color photon burst coincidence analysis.

The detection principle of three-protein interaction (SRC-EGFR-STAT3) with dual-color photon burst coincidence analysis is shown in the figure 47 schematics. To dissect three-protein interaction, we combine the dual-color photon burst coincidence analysis with the one-color two-protein photon burst analysis. There are six characteristic regions delineated by four photon counts boundaries represented by green (QD525) and red (QD605) dotted lines in figure 47. The cartoons placed illustrate the

possible type of protein or protein complex that the single molecule events lying in that region might belong to based on their photon counts and burst coincidence. In other words, single molecule events are plotted in this dual-color photon burst diagram and depending on which region they fall into, we identify these single molecule events as free Qdots, target protein or protein complex. For our experiments, we labeled EGFR with QD605, SRC and STAT3 with QD525. The primary antibodies used to recognize EGFR, SRC and STAT3 (anti-EGFR, anti-SRC and anti-STAT3) are polyclonal in nature. However, to distinguish binding between EGFR with SRC or STAT3, we have to use different animal species for QD525 and QD605. In this case, we chose mouse for QD605, rabbit for QD525 and primary antibodies were also adjusted accordingly. In figure 47, there are four non-coincidence regions, A, B, C and D, and two coincidence regions, E and F. Coincidence events in E and F are identified based on photon burst from red and green channel overlapping in the time domain and these events indicate a complex consisting of both QD525 and QD605 and a potential interaction between target proteins. Events in region A are free QD525 and QD605 in the solution. Since we used the same color QD525 to label both SRC and STAT3 protein, events in region B are identified as either SRC or STAT3 proteins. EGFR is the only protein labeled with QD605, therefore, events in region D are considered as free EGFR proteins. Events in region C have high green counts and these could only be due to interaction between QD525 labeled SRC and STAT3. Finally, events in coincidence region F have both high green and red channel counts, similar in region C, these events could be SRC and STAT3 both interacting with EGFR and forming a complex. Therefore, we consider

events in region F as three-protein interaction events. As for events in region E, where less green counts are observed, we identify them as two-protein interaction, either SRC-EGFR or STAT3-EGFR. In this way, we can effectively categorize molecule events based on their locations on the dual-color photon burst diagram. As a result, number of target protein and protein complex in a particular sample can be identified, thus the interaction dynamics between these target proteins. Unlike the previous experiments with MAXMAD and MYCMAX interaction study, where we transfect DNA into HEK293 cell and over-express MYC, MAX and MAD proteins, in this study, we detect the target protein EGFR, SRC and STAT3 at endogenous level in HeLa tumor cell. HeLa is a well-known and widely-studied cancer cell, which expresses a high level of EGFR proteins. Comparing to transfected HEK293 cell, this study is more clinical relevant in terms of tumor diagnostics and treatment.

The very first step to construct the dual-color photon burst diagram and various boundary conditions to identify protein or protein complex is to define the single QD525 and QD605 boundary counts, same as the approach used in dual-color detection of MYC-MAX interaction in section 7.2. Both Qdots are added into the HeLa cell lysate solution without any primary antibodies and counts boundaries of Qdots are determined based on the three standard deviations from the mean burst counts. EGFR protein can be easily identified with QD605 boundary because it is the only protein being labeled with QD605. However, SRC and STAT3 are both being labeled with QD525, therefore counts boundaries for SRC and STAT3 need to be determined to identify SRC/EGFR/STAT3 complex. Figure 48 A and B show the 2D photon burst diagrams of

SRC and STAT3 samples, where anti-SRC and anti-STAT3 are present in the HeLa cell lysate, respectively. The photon burst boundaries for SRC and STAT3 are determined in the same way by using the three standard deviations from the mean burst counts, indicated as the green dash lines in Figure 48 A and B. We notice the counts boundary for SRC protein is much higher than that of the STAT3. The possible reason could be due to higher affinity or quality of the primary anti-SRC antibody used, which leads to more QD525 binding to SRC target protein. Figure 48 C and D used the same photon burst data of SRC and STAT3 but plotted in the fashion of dual-color photon burst coincidence diagram. As the diagrams suggested, there are few coincidence events detected, which we would categorize as some non-specific binding or detection errors, since there is no anti-EFGR primary antibody present in the solution. Maximum coincidence errors of 1.6% and 0.4% are found for region E and F, respectively. When we quantify protein interaction dynamics in the following step, we will take these errors into consideration.

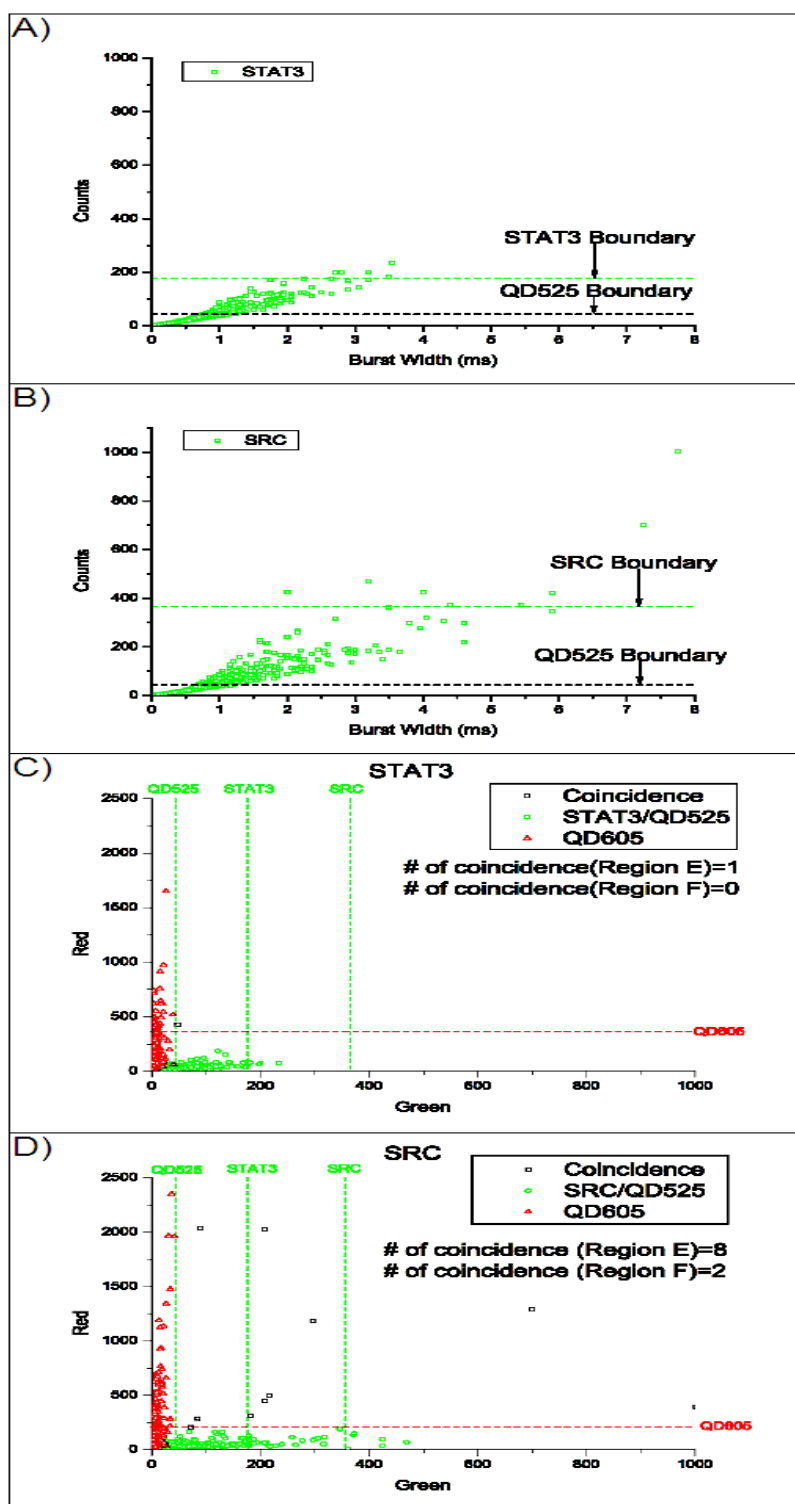


Figure 49 2D photon burst analysis of STAT3 (B) and SRC (A) proteins and dual-color photon burst coincidence analysis of STAT3 (C) and SRC (D).

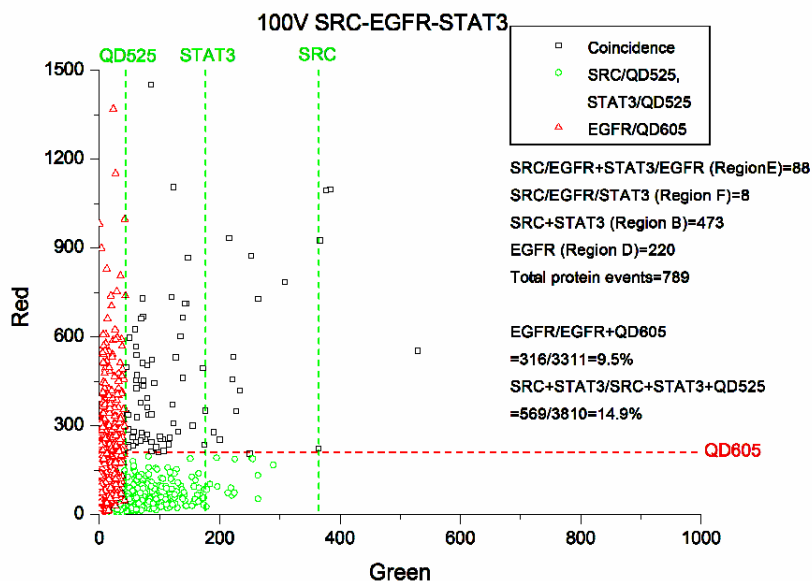


Figure 50 Dual-color photon burst coincidence analysis of SRC/EGFR/STAT3 three-protein interaction.

Now all the photon counts boundary conditions are determined and all six regions in figure 47 schematics are constructed. We test our three-protein detect scheme with sample containing all three primary antibodies, anti-SRC, anti-EGFR and anti-STAT3. The result is shown in figure 49. A total number of 789 protein events are detected. Among them, 220 are identified as EGFR proteins (region D) and 473 are identified as either SRC or STAT3 proteins (region B). In addition, for coincidence events, 88 are identified as two-protein interaction (region E), i.e. STAT3/EGFR or SRC/EGFR, and 8 are identified as three-protein interaction (region F), i.e. SRC/EGFR/STAT3. Then, the protein interaction dynamics can be estimated by the ratio of coincidence events to the total number of protein events. Figure 50 shows the

interaction dynamics between SRC, EGFR and STAT3 proteins in HeLa tumor cell in a bar graph with error bars indicating the lower bounds.

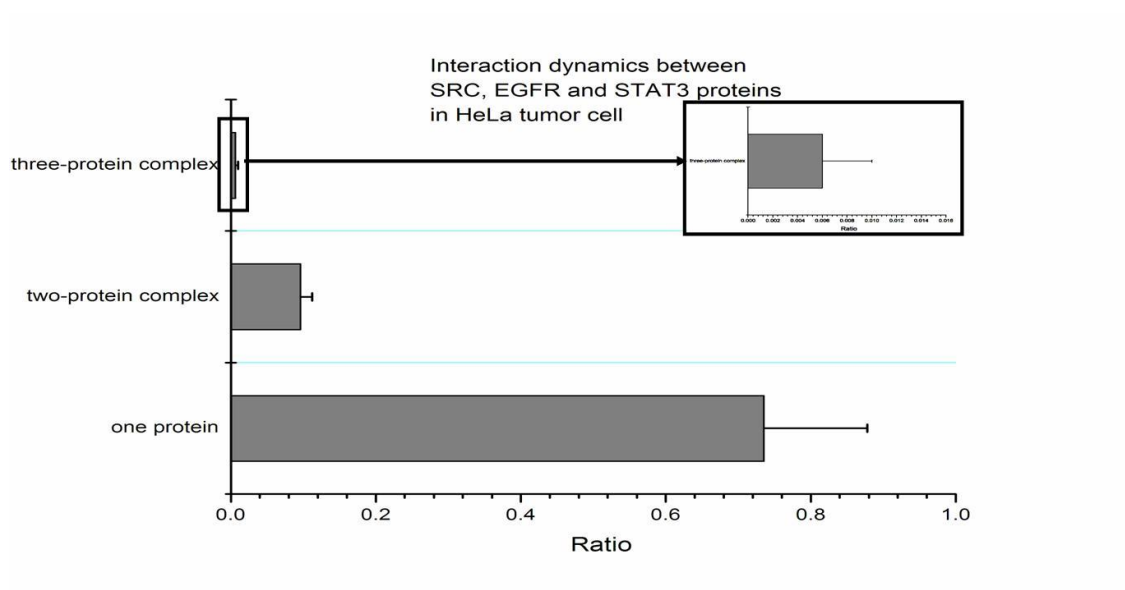


Figure 51 Interaction dynamics between SRC, EGFR and STAT3 proteins in HeLa tumor cell. Inset: magnified three-protein complex ratio. One protein (EGFR, SRC or STAT3), two-protein complex (SRC/EGFR or STAT3/EGFR) and three-protein complex (SRC/EGFR/STAT3), error bar indicates the range.

Errors, including one protein detection error, two-protein and three-protein coincidence errors, are obtained from the previous vector, SRC and STAT3 experiments. For two-protein interaction, a range from 9.6% to 11.2% is obtained. In other words, within the HeLa cell and among all the SRC, STAT3 and EGFR proteins, there is approximately 9.6%-11.2% forming either SRC/EGFR or STAT3/EGFR complex. Furthermore, only 0.6-1% could be forming SRC/EGFR/STAT3 complex. The rest are SRC, STAT3 or EGFR proteins are not forming any complex with a ratio of 73.5-87.8%. It is also worth to notice that no indication is showing the existence of SRC/STAT3

complex because no events are found in region C. This agrees with the current knowledge we have for SRC and STAT3 proteins based on the work with conventional IP technique.

In summary, we have introduced the concept and developed the detection scheme of dual-color photon burst coincidence analysis for studying three-protein interaction. Characteristic protein or protein complex regions are constructed on the dual-color photon burst coincidence diagram to identify the target protein or protein complex. A preliminary study with EGRF, SRC and STAT3 using this technique is demonstrated. The dynamics of two-protein interaction (SRC/EGFR or STAT3/EGFR) and three-protein interaction (SRC/EGFR/STAT3) are estimated based on the number of protein complex identified. This technique not only enables us to achieve fast detection of two-protein interaction, but also can detect three-protein interaction and obtain the interaction dynamics, which are almost impossible with conventional IP assay.

8. CONCLUSIONS AND FUTURE WORKS

8.1 Conclusions

We have developed a novel nanofluidic single molecule detection technique to identify target protein or protein complex direct from cell lysate and at the same time assess the dynamics of protein interactions. Unlike the conventional ensemble measurement assays, we detect single molecule events in a confined nano-scale continuous flow environment. It significantly shortens the detection processing time from 2-3 days for the traditional IP assay to 2-3 minutes with this technique. Another advantage is the ability to quantify certain biological process and protein interaction dynamics with high resolution based on number of single molecule events identified. Furthermore, with this technique, it's possible to detect and assess three-protein interactions, which is very challenging for current conventional immuno-assay techniques.

State-of-the-art top-down silicon and IC processing methods, including photolithography and plasma etching, are used to develop and fabricate the fused silica micro/nano-fluidic channels with widths of $2\mu\text{m}$ and 500nm for single molecule detection. An improved fused silica bonding technique combining temporary bonding with water intermediate layer and permanent high-temperature fusion bonding was successfully developed to achieve a much higher device yield. Due to violent adsorption of positively-charged protein molecule to negatively-charged fused silica surface, it presents a tremendous challenge for researcher working on fluidic protein detection with

fused silica substrate. In this study, we have developed a unique fused silica surface coating protocol to minimize the adsorption due to electro-static interaction between the protein molecule and channel wall. A high-molecular-mass polymer called polyethyleneimine (PEI) is added into the IP buffer solution and this PEI coating solution is introduced into fluidic channel prior to target protein detection. This positively charged polymer adsorbs to the fused silica surface irreversibly and effectively shields the surface from protein molecules. Much higher protein detection efficiency was achieved with this PEI surface coating.

Semiconductor nanoparticles called Quantum dots were used as fluorescent label for our fluorescence-based single molecule detection due to their superb brightness, broad absorption and narrow emission spectrum over conventional organic dyes. Surface functionalized Qdots with secondary antibody attached bind to the target protein through the use of specific target-protein-recognizing polyclonal primary antibodies. The main detection strategy for our technique is the polyclonal nature of the primary antibodies, which are able to bind to the target protein at a number of epitopes. This leads to the association of multiple Qdots with one target protein and yields a much higher photon burst counts for target protein events comparing to free Qdots in the solution. As a result, we are able to distinguish and count the number of target protein events by comparing the photon counts of each individual burst events from the sample containing target protein molecules to those of the control sample. For all our target protein and protein interaction detection experiments, the samples are under the equilibrium condition of antibody hybridization.

Surface modified fused silica micro/nano-fluidic channels and the 2D photon burst analysis methods were first characterized with free Qdots in IP buffer solution, including flow velocity as a function of applied voltage and concentration analysis of Qdots. Then, we have successfully demonstrated the detection of target protein HA epitope tagged MAX direct from cell lysate with the 2D photon burst analysis. To validate our target protein detection approach, we analyzed the cell lysate samples containing different concentrations of MAX protein. An excellent linear relationship is found for the number of MAX events as a function of MAX concentration. More importantly, we have shown the detection of two-protein interaction with both one-color and dual-color photon burst analysis approaches. MAD-MAX interaction was detected by using only one Qdot. MAD and MAX were both labeled with QD525 and the interaction was identified based on a higher photon count of MAD-MAX complex than those of MAX or MAD protein alone. A binding ratio of 7%-10% was found for MAD-MAX interaction among all the MAX and MAD proteins. In a similar fashion, we were able to detect the interaction between MYC and MAX proteins with QD605 and a binding ratio of 7%-8.1% was found for MYC-MAX interaction. To confirm this binding ratio, we performed a dual-color detection to study the same MYC-MAX interaction, where MYC is labeled with QD605 and MAX is labeled with QD525. MYC-MAX complex is identified based on the coincidence events in terms of red (QD605) and green (QD525) channels. A binding ratio of 6.8%-8.2% was found for the dual-color detection for MYC-MAX, which is in very good agreement with the one-color detection.

Last but not least, a preliminary study of three-protein interaction was demonstrated by combining the one-color photon burst analysis and dual-color photon burst coincidence analysis. A tumor signal transduction-related membrane protein called EGFR is known to interact with both SRC and STAT3 proteins in HeLa cancer cell. A binding ratio of 9.6-11.2% was found for two-protein SRC/EGFR and STAT3/EGFR interaction and 0.6-1% was found for SRC/EGFR/STAT3 interaction.

In summary, we have successfully developed an efficient nanofluidic single molecule detection technique for target protein detection and protein interaction study. Interaction dynamics in terms of binding ratio among proteins of interest can be obtained as well as three-protein interaction studies.

8.2 Future works

We have described a powerful nanofluidic single molecule detection technique for protein detection and interaction study and shown the promising results from proof-of-principle experiments. However, this technique is still in its very early stage of development. Improvements related to many aspects of this technique and studies of different are necessary: 1) Design redundant parallel 500nm-wide nanofluidic channel to improve device robustness due to Qdot adsorption and clogging within the detection volume. 2) Characterize the PEI coating protocol in terms of PEI concentration and coating time to achieve maximum performance. 3) Installation of the three-channel detection system replacing the current two-channel system from ISS. With the three-channel detection system, three-protein interaction study becomes more straightforward

and interactions between up to six molecules are possible with the technique described in this work. 4) Concentration analysis of EGFR protein: A) Analysis of EGFR concentration in HEK293 cell at different level of DNA expression. B) Compare the endogenous level EGFR concentration in MCF7, HeLa and 468 tumor cells, which express EGFR at a different level based on conventional IP studies. 5) Compare the interaction dynamics of EGFR with SRC and STAT3 proteins in HeLa tumor cell with MCF7 and 468 tumor cells. 6) Target proteins are labeled with Qdots through specific target-recognizing primary antibodies in this study. However, the success of experiments highly relies on the quality of primary antibody chosen. A better alternative is to direct conjugate the Qdots to the target protein with the use of commercial available conjugation kit.

REFERENCES

- 1 L. A. Gloeckler Ries, M. E. Reichman, D. R. Lewis, B. F. Hankey and B. K. Edwards, *Oncologist*, 2003, **8**, 541.
- 2 C. I. Bargmann, M. C. Hung and R. A. Weinberg, *Nature*, 1986, **319**, 226.
- 3 M. C. Hung, A. L. Schechter, P. Y. Chevray, D. F. Stern and R. A. Weinberg, *Proc. Natl. Acad. Sci. U.S.A.*, 1986, **83**, 261.
- 4 D. Yu and M. C. Hung, *Oncogene*, 2000, **19**, 6115.
- 5 B. P. Zhou, Y. Liao, W. Xia, Y. Zou, B. Spohn and M. C. Hung, *Nat. Cell Biol.*, 2001, **3**, 973.
- 6 J. Momand, H. H. Wu and G. Dasgupta, *Gene*, 2000, **242**, 15.
- 7 M. S. Colman, C. A. Afshari and J. C. Barrett, *Mutat. Res.*, 2000, **462**, 179.
- 8 R. Honda and H. Yasuda, *Embo. J.*, 1999, **18**, 22.
- 9 S. Weiss, *Science*, 1999, **283**, 1676.
- 10 S. Weiss, *Nature Structural Biology*, 2000, **7(9)**, 724.
- 11 B. Rotman, *Proc. Natl. Acad. Sci. U.S.A.*, 1961, **47**, 1981.
- 12 J. Enderlein, *Fluorescence in Biology*, Springer, Berlin, 2006.
- 13 J. Enderlein, W. P. Ambrose, P. M. Goodwin and R. A. Keller, *Microsystem Technology: A Powerful Tool for Biomolecular Studies: Fluorescence Detection of Single Molecules Applicable to Small Volume Assays*, Birkhäuser, Basel, Switzerland, 1999.
- 14 A. J. de Mello, *Lab Chip*, 2003, **3**, 29N.

- 15 E. B. Shera, N. K. Seitzinger, L. M. Davis, R. A. Keller and S. A. Soper, *Chem. Phys. Lett.*, 1990, **174**, 553.
- 16 G. Whiteside, *Nature*, 2006, **442**, 368.
- 17 A. Manz, D. J. Harrison, E. M. J. Verpoorte, J. C. Fettinger, A. Paulus, H. Ludi and H. M. Widmer, *J. Chromatog.*, 1992, **593**, 253.
- 18 H. A. Stone, A. D. Stroock and A. Ajdari, *Annu. Rev. Fluid. Mech.*, 2004, **36**, 381.
- 19 F. K. Balagaddé L. You, C. L. Hansen, F. H. Arnold and S. R. Quake, *Science*, 2005, **309**, 137.
- 20 D. R. Reyes, D. Iossifidis, P.-A. Auroux and A. Manz, *Anal. Chem.*, 2002, **74**, 2623.
- 21 P.-A. Auroux, D. Iossifidis, D. R. Reyes and A. Manz, *Anal. Chem.*, 2002, **74**, 2637.
- 22 T. Vilkner, D. Janasek and A. Manz, *Anal. Chem.*, 2004, **76**, 3373.
- 23 J. O. Tegenfeldt, C. Prinz, H. Cao, R. L. Huang, R. H. Austin, S. Y. Chou, E. C. Cox and J. C. Sturm, *Anal. Bioanal. Chem.*, 2004, **378**, 1678.
- 24 T. M. Squires and S. R. Quake, *Reviews of Modern Physics*, 2005, **77**, 977.
- 25 D. J. Beebe, G. A. Mensing and G. M. Walker, *Annu. Rev. Biomed. Eng.*, 2002, **4**, 261.
- 26 <http://www.micron.com/k12/semiconductors/photo>, date accessed: Dec. 2008
- 27 D. Mijatovic, J. C. T. Eijkel and A. van den Berg, *Lab Chip*, 2005, **5**, 492.
- 28 S. M. Stavis, J. B. Edel, K. T. Samiee and H. G. Craighead, *Lab Chip*, 2005, **5**, 337.
- 29 P. Mao and J. Han, *Lab Chip*, 2005, **5**, 837.

- 30 H. Cao, Z. N. Yu, J. Wang, J. O. Tegenfeldt, R. H. Austin, E. Chen, W. Wu and S. Y. Chou, *Appl. Phys. Lett.*, 2002, **81**, 174.
- 31 M. Foquet, J. Korlach, W. Zipfel, W. W. Webb and H. G. Craighead, *Anal. Chem.*, 2002, **74**, 1415.
- 32 W. L. Li, J. O. Tegenfeldt, L. Chen, R. H. Austin, S. Y. Chou, P. A. Kohl, J. Krotine and J. C. Sturm, *Nanotechnology*, 2003, **14**, 578.
- 33 C. K. Harnett, G. W. Coates and H. G. Craighead, *J. Vac. Sci. Technol. B*, 2001, **19**, 2842.
- 34 J. C. McDonald, D. C. Duffy, J. R. Anderson, D. T. Chiu, H. K. Wu, O. J. A. Schueller and G. M. Whitesides, *Electrophoresis*, 2000, **21**, 27.
- 35 M. L. Chabinyk, D. T. Chiu, J. C. McDonald, A. D. Stroock, J. F. Christian, A. M. Karger and G. M. Whitesides, *Anal. Chem.*, 2001, **73**, 4491.
- 36 L. J. Guo, *J. Phys.D: Appl. Phys.*, 2004, **37**, R123.
- 37 L. J. Guo, X. Cheng and C. F. Chou, *Nano Lett.*, 2004, **1**, 69.
- 38 S. Y. Chou, P. R. Krauss and P. J. Renstrom, *Appl. Phys. Lett.*, 1995, **67(21)**, 20.
- 39 D. Li and Y. N. Xia, *Nano Lett.*, 2004, **5**, 933.
- 40 M. Wang, N. Jing, C. B. Su, C. K. Chou, M. C. Hung, K. A. Chang and J. Kameoka, *J. Appl. Phys. Lett.*, 2006, **88**, 033106.
- 41 D. A. Czaplewski, J. Kameoka, R. Mathers, G. W. Coates and H. G. Craighead, *Appl. Phys. Lett.*, 2003, **83(23)**, 4836.
- 42 B. Ilic, D. Czaplewski, M. Zalalutidinov, B. Schmidt and H. G. Craighead, *J. Vac. Sci. Technol. B*, 2002, **20**, 2459.

- 43 N.-T. Nguyen and S. T. Wereley, *Fundamentals and Applications of Microfluidics*, Artech House, Boston, MA, 2002.
- 44 M. J. Madou, *Fundamentals of Microfabrication: The Science of Miniaturization*, CRC Press, Boca Raton, FL, 1997.
- 45 J. L. Perry and S. G. Kandlikar, *Microfluid Nanofluid*, 2006, **2**, 185.
- 46 P. S. Dittrich and A. Manz, *Anal. Bioanal. Chem.*, 2005, **382**, 1771.
- 47 H. Craighead, *Nature*, 2006, **442**, 387.
- 48 J. T. Mannion and H. G. Craighead, *Biopolymer*, 2006, **85(2)**, 131.
- 49 J. Han and H. G. Craighead, *J. Vac. Sci. Technol. A*, 1999, **17(4)**, 2142.
- 50 J. Han and H. G. Craighead, *Science*, 2000, **288**, 1026.
- 51 S. W. Turner, A. M. Perez, A. Lopez and H. G. Craighead, *J. Vac. Sci. Technol. B*, 1998, **16(6)**, 3835.
- 52 B. B. Haab and R. A. Mathies, *Anal. Chem.*, 1999, **71**, 5137.
- 53 J. Knemeyer, N. Marmé and M. Sauer, *Anal. Chem.*, 2000, **72**, 3717.
- 54 E. Y. Chan, N. M. Goncalves, R. A. Haeusler, A. J. Hatch, J. W. Larson, A. M. Maletta, G. R. Yantz, E. D. Carstea, M. Fuchs, G. G. Wong, S. R. Gullans and R. Gilmanshin, *Methods*, 2004, **14**, 1137.
- 55 J. W. Larson, G. R. Yantz, Q. Zhong, R. Charnas, C. M. D'Antoni, M. V. Gallo, K. A. Gillis, L. A. Neely, K. M. Phillips, G. G. Wong, S. R. Gullans, R. Gilmanshin, *Lab Chip*, 2006, **6**, 1187.
- 56 H. P. Chou, C. Spence, A. Scherer and S. Quake, *Proc. Natl. Acad. Sci. U.S.A.*, 1999, **96**, 11.

- 57 R. Riehn, M. Lu, Y. Wang, S. F. Lim, E. C. Cox and R. H. Austin, *Proc. Natl. Acad. Sci. U.S.A.*, 2005, **102**, 10012.
- 58 J. T. Mannion, C. H. Reccius, J. D. Cross and H. G. Craighead, *Biophysical Journal*, 2006, **90**, 4538.
- 59 S. W. Turner, P. M. Cabodi and H. G. Craighead, *Phys. Rev. Lett.*, 2002, **88**, 128103.
- 60 A. van Orden, N. P. Machara, P. M. Goodwin and R. A. Keller, *Anal. Chem.*, 1998, **70**, 1444.
- 61 S. M. Stavis, J. B. Edel, Y. Li, K. T. Samiee, D. Luo and H. G. Craighead, *Nanotechnology*, 2005, **16**, S314.
- 62 M. Gosch, H. Blom, J. Holm, T. Heino and R. Rigler, *Anal. Chem.*, 2000, **72**, 3260.
- 63 P. M. Goodwin, R. L. Nolan and H. Cai, *Current Pharmaceutical Biotechnology*, 2004, **5**, 271.
- 64 H. Li, L. Ying, J. J. Green, S. Balasubramanian and D. Klenerman, *Anal. Chem.*, 2003, **75**, 1664.
- 65 H. Li, D. Zhou, H. Browne, S. Balasubramanian and D. Klenerman, *Anal. Chem.*, 2004, **76**, 4446.
- 66 J. Widengren, V. Kudryavtsev, M. Antonik, S. Berger, M. Gerken and C. A. M. Seidel, *Anal. Chem.*, 2006, **78**, 2039.
- 67 D. Kim, Y.-G. Kwak and S. Kang, *Analytica Chimica Acta*, 2006, **577**, 163.
- 68 J. Elf, G.-W. Li and X. S. Xie, *Science*, 2007, **316**, 1191.
- 69 A. Pramanik, *Current Pharmaceutical Biotechnology*, 2004, **5**, 205.

- 70 L. Li, S. Chen, S. Oh and S. Jiang, *Anal. Chem.*, 2002, **74**, 6017.
- 71 A. J. W. G. Visser, B. H. Kunst, H. Keller and A. Schots, *Current Pharmaceutical Biotechnology*, 2004, **5**, 173.
- 72 A. Agrawal, C. Zhang, T. Byassee, R. A. Tripp and S. Nie, *Anal. Chem.*, 2006, **78**, 1061.
- 73 A. Castro and J. G. K. Williams, *Anal. Chem.*, 1997, **69**, 3915.
- 74 C.-Y. Zhang and L. W. Johnson, *Analyst*, 2006, **131**, 484
- 75 D. B. Woods and K. H. Vousden, *Exp. Cell Res.*, 2001, **264**, 56.
- 76 C. J. Sherr and J. D. Weber, *Curr. Opin. Genet. Dev.*, 2000, **10**, 94.
- 77 B. Vogelstein, D. Lane and A.J. Levine, *Nature*, 2000, **408**, 307.
- 78 <http://www.molecularstation.com/fi/protein/immunoprecipitation/>, date accessed: Dec. 2008.
- 79 Z.-J. Jia, Q. Fang and Z.-L. Fang, *Anal. Chem.*, 2004, **76**, 5597.
- 80 G. Karniadakis, A. Beşkök and N. R. Aluru, *Microflows and Nanoflows*, Springer, New York, 2005.
- 81 E. A. S. Doherty, R. J. Meagher, M. N. Albarghouthi and A. E. Barron., *Electrophoresis*, 2003, **24**, 34.
- 82 F. B. Erim, A. Cifuentes, H. Poppe and J. C. Kraak, *Journal of Chromatography A*, 1995, **708**, 356.
- 83 X. Michalet, F. F. Pinaud, L. A. Bentolila, J. M. Tsay, S. Doose, J. J. Li, G. Sundaresan, A. M. Wu, S. S. Gambhir and S. Weiss, *Science*, 2005, **307**, 539.

- 84 D. R. Larson, W. R. Zipfel, R. M. Williams, S. W. Clark, M. P. Bruchez, F. W. Wise and W. W. Webb, *Science*, 2003, **300**, 1434.
- 85 A. P. Alivisatos, *Science*, 1996, **271**, 933.
- 86 <http://www.invitrogen.com/site/us/en/home.html>, date accessed: Dec. 2008.
- 87 <http://www.chroma.com/>, date accessed: Dec. 2008.
- 88 O. Krichevsky and G. Bonnet, *Rep. Prog. Phys.*, 2002, **65**, 251.
- 89 W. W. Webb, *Applied Optics*, 2001, **40**, 3969.
- 90 S. T. Hess, S. Huang, A. A. Heikal and W. W. Webb, *Biochemistry*, 2002, **41**, 697.
- 91 M. A. Medina and P. Schwille, *BioEssays*, 2002, **24**, 758.
- 92 P. Schwille and E. Haustein, *Fluorescence Correlation Spectroscopy: An Introduction to Its Concepts and Applications*, Max-Planck-Institute for Biophysical Chemistry, Berlin, 2004.
- 93 M. Foquet, J. Korlach, W. R. Zipfel, W. W. Webb and H. G. Craighead, *Anal. Chem.*, 2004, **76**, 1618.
- 94 J. Enderlein, D. L. Robbins, W. P. Ambrose, P. M. Goodwin and R. A. Keller, *Bioimaging*, 1997, **5**, 88.
- 95 D. R. Baker, *Capillary Electrophoresis*, John Wiley & Sons, Inc., New York, 1995.

APPENDIX A

Microfluidic Channel Fabrication Process Flow

A. Contact lithography for 2 μ m-wide channel

4" UV-grade fused silica wafer, double sided polished, 500- μ m thick

1. Dispense P-20 primer and let it sit for 5 seconds
2. Spin coat P-20 primer at 4000rpm (ramp 2000rpm/s) for 45 seconds
3. Spin coat photoresist S1818 at 4000rpm (ramp 2000rpm/s) for 45 seconds
4. Softbake on a hotplate at 115 °C for 1 minute
5. EV620 contact aligner (soft contact) and expose for 4 seconds
6. MIF 300 develop for 1 minute
7. Hardbake at 115 °C for 1 minute
8. Descum in Branson Barrel Etcher for 4 minutes (@ room temperature)
9. Oxford 82 (MOS clean) oxygen plasma clean (60mTorr, 50 SCCM O₂, 150W) for 15 minutes
10. Oxford 82 (MOS clean) CF₄ chamber-seasoning for 5 minutes
11. Oxford 82 (MOS Clean) CF₄ etch (40mTorr, 20SCCM CF₄, 150W) fused silica for
25 minutes (~500nm)
10 minutes (~200nm)
2.5 minutes (~50nm)
12. Remove photoresist with oxygen plasma for 15 minutes in Oxford 82
13. Clean wafer with hot piranha
14. Spin coat P-20 and FSC-M at 3000rpm (ramp 1000rpm/s) for 1 minute

15. Air oven bake at 90 °C for 30 minutes
16. Alumina power sand blaster to create fluid access holes on fused silica wafer
17. Remove FSC-M in resist strip hot bath for 30 minutes
18. Clean wafer with hot piranha, both substrate and cover wafer
19. Cover both substrate and cover wafer with de-ionized water and bring two together to form a temporary bonding
20. Let the bonded wafer sit for 3 days and water evaporates
21. Thermal fusion bonding at 1100 °C for 7 hours in air furnace

B. Projection lithography for 500nm-wide channel

4" UV-grade fused silica wafer, double sized polished, 500- μ m thick

1. Dispense P-20 primer and let it sit for 5 seconds
2. Spin coat P-20 primer at 4000rpm (ramp 2000rpm/s) for 45 seconds
3. Spin coat SPR700 1.2L at 6000rpm (ramp 8000rpm/s) for 45 seconds
4. Softbake on a hotplate at 95 °C for 2 minutes
5. Autostepper (GCA AS200) expose for 0.12 seconds with focus of +6
6. Post exposure bake on a hotplate at 115 °C for 1 minute
7. MIF 300 develop for 1 minute
8. Hardbake on a hotplate at 90 °C for 30 minutes
9. Descum in Branson Barrel Etcher for 4 minutes (@ room temperature)
10. Oxford 82 (MOS clean) oxygen plasma clean for 15 minutes and CF₄ seasoning for 5 minutes

11. Oxford 82 (MOS Clean) CF_4 etch (40mTorr, 20 SCCM CF_4 , 150W) fused silica
for 25 minutes (~500nm)
 10 minutes (~200nm)
 2.5 minutes (~50nm)
12. Remove photoresist with oxygen plasma for 5 minutes in Oxford 82
13. Clean wafer with hot piranha
14. Spin coat P-20 and FSC-M at 3000rpm (ramp 1000rpm/s) for 1 minute
15. Air oven bake at 90 °C for 30 minutes
16. Alumina power sand blaster to create fluid access holes on fused silica wafer
17. Remove FSC-M in resist strip hot bath for 30 minutes
18. Clean wafer with hot piranha, both substrate and cover wafer
19. Cover both substrate and cover wafer with de-ionized water and bring two
together to form a temporary bonding
20. Let the bonded wafer sit for 3 days and water evaporates
21. Thermal fusion bonding at 1100 °C for 7 hours in air furnace

APPENDIX B

Target protein HAMAX concentration analysis

In section 6, we presented the detection of target HAMAX protein direct from cell lysate and its concentration analysis with 2D photon burst diagram. We varied the concentration of HAMAX by adjusting the amount of transfection DNA injected into the HEK293 cell. Here, we present another concentration analysis of HAMAX protein and we varied the concentration of HAMAX by simply changing the concentration of cell lysate in IP binding buffer solution.

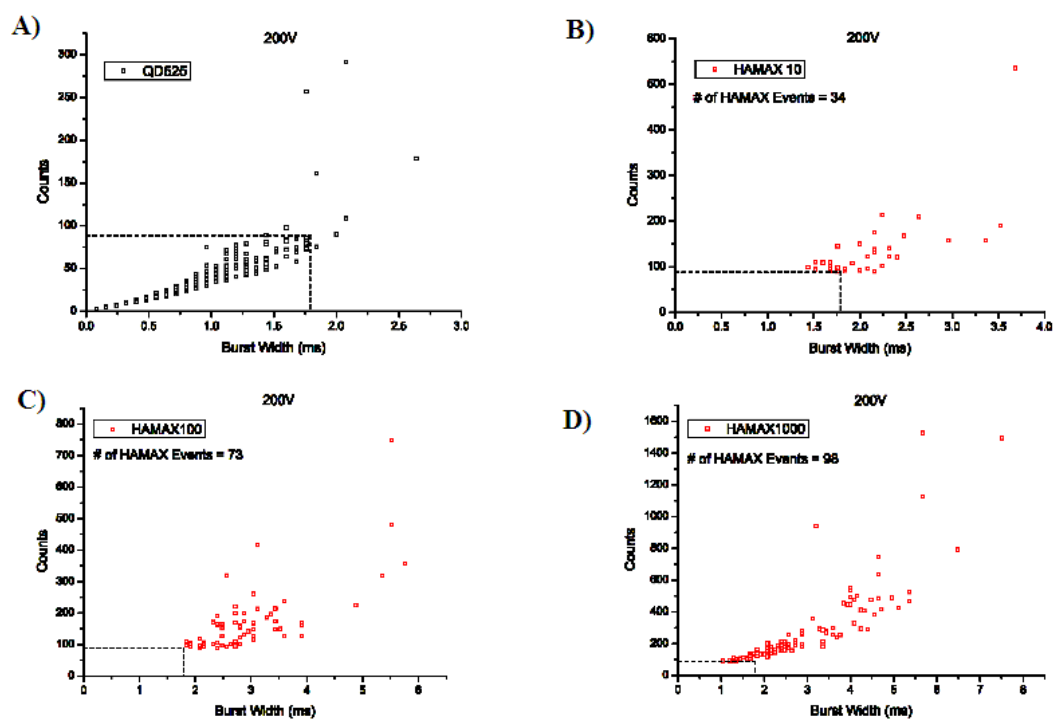


Figure 52 2D photon burst diagrams of HAMAX sample with different lysate concentrations. A) Determination of QD525 boundary in terms of burst width and photon counts; B, C, D) HAMAX 10, HAMAX 100 and HAMAX 1000 events plotted with QD525 boundary showing increase of number of HAMAX events.

Three samples with 10 μ g protein lysate in 1ml IP buffer (HAMAX 10), 100 μ g protein lysate in 1ml IP buffer (HAMAX 100) and 1000 μ g protein lysate in 1ml IP buffer (HAMAX 1000) were prepared using the same HEK293 cell lysate.

The same 2 μ m-wide microchannel, 200V and 2D photon burst analysis were used for this experiment. A characteristic region is first identified for QD525 in IP buffer solution with vector cell lysate (HAMAX not over-expressed) as control, as shown in figure 51A. With this boundary, 2D photon burst plots of target HAMAX protein at various concentrations are generated, as shown in figure 51B, 51C, 51D (events within the QD525 boundary are not plotted). Events, which locate outside of the QD525 boundary on figure 51A, are statistically considered as HAMAX events. A total number of 34, 73 and 98 HAMAX events are detected for concentrations of 10 μ g/ml, 100 μ g/ml and 1000 μ g/ml, respectively. More HAMAX events with significantly high photon counts are found in high concentration sample, such as the one with 1000 μ g/ml. As concentration increases, the possibility of HAMAX forming dimer increases as well. HAMAX dimer will lead to even higher photon counts comparing to HAMAX monomer. Figure 52 shows the linear fit of the events of HAMAX 10 μ g/ml, 100 μ g/ml and 1000 μ g/ml and error bar is the standard deviation from 3 independent measurements. More experiments are still underway to investigate the abnormally high standard deviation for HAMAX 100 μ g/ml sample.

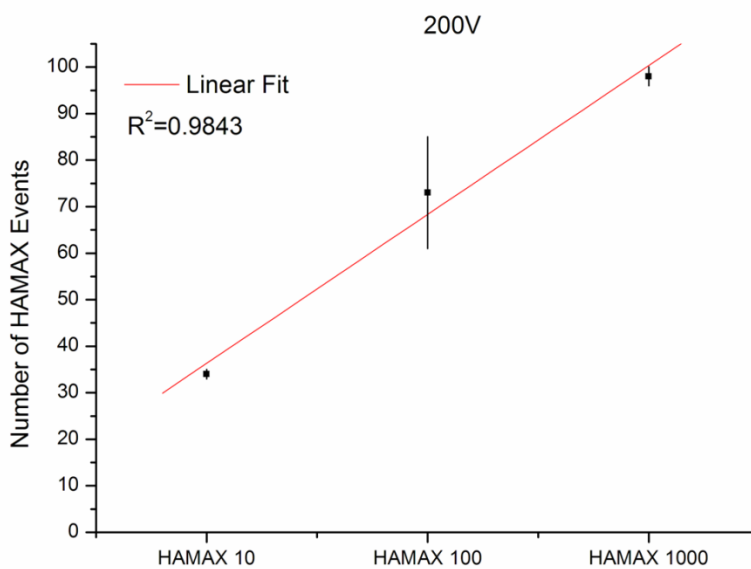


Figure 53 Number of HAMAX events as a function of HAMAX lysate concentration. HAMAX 10 (10 μ g/ml), HAMAX 100 (100 μ g/ml) and HAMAX 1000 (1000 μ g/ml), error bar indicates the standard deviation.

APPENDIX C

MATLAB code for two-dimensional photon burst analysis

All data analysis is performed with MATLAB software version 7.1.

load rawdata.txt A=rawdata;	Load raw data file in ascii format
B=A(:,2);	Load count column into B
C=tsmovavg(B,'s',10,1); C=C(10:size(C));	Perform simple moving average on B with moving window of 10
D=3*sqrt(mean(C))+mean(C);	Find counts threshold D with 3 standard deviations from the mean
E=[find(C>D), C(find(C>D))];	Find all the data points in C with counts higher than threshold D and return the these data points in matrix E
F=[0,0];s=E(1,1); for n=1:length(E)-1 if E((n+1),1)>E(n,1)+1 t=E(n,1); a=t-s+1;b=sum(C(s:t)); F=[F;a*(raw data bin time)/1000,b]; s=E(n+1,1); end end	Scan matrix E and find data points that are continuous in time. Combine these data points to get the burst width and photon count of one molecule event. All events are recorded in matrix F with left column of burst width and right column of photon counts
save results.txt F -ascii	Output results in results.txt file in ascii format

VITA

Name: Nan Jing

Address: Department of Electrical and Computer Engineering
c/o Dr. Jun Kameoka
Texas A&M University
College Station, TX 77843-3128
USA

Email: njing@tamu.edu

Education: B.S., Materials Science and Engineering, Southeast University, Nanjing, China, 2001
M.S., Materials Science and Engineering, Case Western Reserve University, Cleveland, OH, 2003
Ph.D. Electrical and Computer Engineering, Texas A&M University, College Station, TX, 2009